

LA-UR-24-24588

Approved for public release; distribution is unlimited.

Title: Modelling Inter- and Intra-granular Dislocation Transport using Crystal Plasticity

Author(s): Chakraborty, Subhendu
Hunter, Abigail
Luscher, Darby Jon

Intended for: International Journal of Plasticity

Issued: 2024-05-09 (Draft)



Los Alamos National Laboratory, an affirmative action/equal opportunity employer, is operated by Triad National Security, LLC for the National Nuclear Security Administration of U.S. Department of Energy under contract 89233218CNA00001. By approving this article, the publisher recognizes that the U.S. Government retains nonexclusive, royalty-free license to publish or reproduce the published form of this contribution, or to allow others to do so, for U.S. Government purposes. Los Alamos National Laboratory requests that the publisher identify this article as work performed under the auspices of the U.S. Department of Energy. Los Alamos National Laboratory strongly supports academic freedom and a researcher's right to publish; as an institution, however, the Laboratory does not endorse the viewpoint of a publication or guarantee its technical correctness.

Modelling Inter- and Intra-granular Dislocation Transport using Crystal Plasticity.

Subhendu Chakraborty ¹, Abigail Hunter ², D.J. Luscher ²

¹ Theoretical Division, Los Alamos National Laboratory, Los Alamos, NM,
USA

² X-Computational Physics Division, Los Alamos National Laboratory, Los
Alamos, NM, USA
May 7, 2024

Abstract

This work presents the development of a crystal plasticity material model that incorporates dislocation transport both within the grain and across the grain boundary. The model accounts for both local and non-local evolution of dislocation density. The dislocation transport is modelled using the advection equation with source term, which represents local evolution of the dislocations. Non-local dislocation evolution, or flux, is realized via the physical transport of dislocation within the grain and transfer of dislocations across the grain boundary. A novel geometry based criterion is developed to determine the direction of dislocation transfer across grain boundaries. The transfer criterion incorporates the geometric features of the grain boundary, such as the grain boundary plane normal, and its misorientation, which is accounted for through the orientation of the incoming and outgoing slip systems. In addition, the transfer criterion also accounts for the local stress state of the material near the grain boundary. As part of this effort, this crystal plasticity model has been implemented in the open-source finite element code MOOSE. The development of the transfer criterion, implementation of the model, and its application to single crystal, bi-crystal and polycrystal samples of copper are discussed in detail.

1 Introduction

Dislocation accommodated plasticity plays an important role in the deformation of most crystalline materials. In metallic materials, movement of dislocations play a critical role in the plastic flow, and accumulation of plastic strain within the material. Due to this, it might be appropriate for any material model at mesoscale to incorporate dislocation transport within grains as well as across grain boundaries for polycrystalline metallic materials.

Development in microscopy technology has provided images which show that the interaction of dislocations with grain boundaries can play a major role in the plastic

deformation of metals and the range of viable interactions is more complex than these bounding cases of GBs being fully transparent or opaque to dislocation transfer [1, 2, 3, 4]. These observations motivate the development of a crystal plasticity model that incorporates the physical transport of dislocations both within the grains and across grain boundaries. The model should also incorporate the dependence of dislocation transfer across the GB on the geometric features of grains on either side of a GB, the GB plane, and the local state of material adjacent to the GB, e.g., the resolved shear stress, and dislocation density.

Over the years, many crystal plasticity models are developed to model the plasticity in metallic materials. A detailed overview of such models can be found in [5]. In some of these models, the dislocation transport is incorporated implicitly in the sense that the effect of dislocation movement, i.e. development of plastic strain, is computed either by using a phenomenological shearing rate[6, 7] or by using a model describing the mean dislocation velocity [8, 9]. In these continuum crystal plasticity models dislocations are not physically transported.

On the other hand in a separate class of continuum crystal plasticity theory, the spatial evolution of dislocation density fields represent the consequence of the transport of dislocations throughout the lattice across the material and is a part of the solution variables [10, 11]. In these second class of continuum crystal plasticity material models, the movement of dislocations within the grain is mainly influenced by the resolved shear stress, a relatively long-ranged backstress associated with the polarization of the dislocation density field, and the local hardening of the material due to dislocation reaction and/or dislocation segregation. Across grain boundaries (GBs), it is often assumed that the GB is either completely transparent to a passing dislocation i.e., 100% transfer of dislocations across the GB, or opaque to dislocations, i.e., no transfer across the GB at all. In [12, 13] the effect of slip transfer across the grain boundary(GB) is explored using a density based crystal plasticity model. In this model, the effect of dislocation transfer across the GBs is realized by modifying the dislocation source term in the vicinity of the GBs that causes the dislocation accumulation near the GBs.

In the present work, we build upon the crystal plasticity model that was developed in [10, 11]. This dislocation-density based crystal plasticity model comprises the coupled evolution of three modules: the Deformation Momentum Balance (DMB), the Continuum Dislocation Transport (CDT), and the Dislocation Deformation Compatibility (DDC). The DMB component of the model describes classical continuum deformation field theory, with the displacement field as the primary unknown variable, and is governed by the principle of conservation of momentum under the applied loading. The CDT component of the model describes the conservation laws for the densities of dislocation populations which are treated as primary field variables. Finally, the DDC sub-problem reconciles evolving dislocation fields from CDT with the deformation and stress fields of DMB. Specifically, solving the DDC sub-problem is necessary to identify the long-range residual stress field, and associated strain field, attributed to the distribution of non-redundant dislocations in the lattice [14, 15, 16].

This model was previously published with application to high rate loading conditions [10, 11]. In this previous effort, key advances in the model development included an explicit representation of dislocation transport (CDT), detailed accounting for elastic interactions involving geometrically necessary dislocations (DDC), classical momentum balance (DMB), and the tight coupling between all three of these sub-problems.

This previous model considered GBs to be either fully transparent or opaque to the flux of dislocations.

Here we present an implementation that can be applied to low rate and quasi-static loading conditions. We use the open-source finite-element library ‘Multiphysics Object Oriented Simulation Environment’ (MOOSE) [17] as the base code. MOOSE is an open-source finite element framework developed in C++ at Idaho National Laboratory. The modular structure of MOOSE makes it convenient to incorporate new physics including new constitutive theories or additionally coupled partial differential equations within it. The integration of MOOSE with PETSc [18, 19] makes it convenient to leverage various efficient non-linear solvers. The ‘DiscoFlux’ material model is implemented within the MOOSE framework using a semi-implicit solution strategy for each sub-component. Additionally, we have expanded the CDT sub-problem and solution to account for dislocation transport both within grains and across grain boundaries when modeling polycrystalline materials. A novel dislocation transfer model across the GB is developed that incorporates the fact that the transfer of dislocation can happen between dislocation of same polarity as well as of opposite polarity. This fact was previously ignored in the existing literatures. To put these advances into context, we first present a brief summary of key equations in the DMB and DDC modules in Sections 2.1 and 2.2. The CDT module is described in more detail in Section 2.3. Simulation results to demonstrate the applicability of this new model are presented for single crystal, bi-crystal and polycrystal numerical test problems presented in Section 3.

2 Computational methodology

2.1 Deformation Momentum Balance (DMB)

The governing differential equation to model the deformation of a deformable body is obtained by imposing the conservation of linear momentum and can be expressed as,

$$\nabla_0 \cdot \mathbf{P} = \rho_0 \ddot{\mathbf{x}} \quad (1)$$

where \mathbf{P} is the first Piola-Kirchhoff stress, $\mathbf{x} = \phi(t, \mathbf{X})$ is the deformed position vector of the material point within the body which originally coincided with the position \mathbf{X} of the same material point in the undeformed reference configuration, t is time, and ϕ is the mapping function from the reference configuration to the current or deformed configuration. ρ_0 is the density of the material in the undeformed configuration. In the present work, we focus on problems with a slow rate of deformation consistent with quasi-static conditions, and therefore omit the inertia term in equation 1 enabling rewriting as

$$\nabla_0 \cdot \mathbf{P} = 0. \quad (2)$$

2.1.1 Kinematics

Finite deformation kinematics employed here include deformation modes associated with elastic stretching of the lattice, crystal lattice rotation, and plastic slip. The deformation gradient \mathbf{F} admits a multiplicative decomposition into elastic and plastic

Variable Name	Definition
\mathbf{S}	First Piola-Kirchhoff stress
$\hat{\mathbf{S}}$	Second Piola-Kirchhoff stress
σ	Cauchy stress
ρ_0	Mass density of the material in reference configuration
\mathbf{F}	Deformation gradient
\mathbf{F}_e	Elastic part of \mathbf{F}
\mathbf{F}_p	Plastic part of \mathbf{F}
\mathbf{L}	Velocity gradient
\mathbf{L}_p	Plastic part of \mathbf{L}
$\dot{\gamma}$	Plastic shearing rate
\mathbf{s}_0	Slip direction in reference configuration
\mathbf{n}_0	Slip plane normal in reference configuration
\mathbf{S}_0	Schmid tensor in reference configuration
\mathbf{E}_e	Elastic Green-Lagrange strain
ρ_e^α	Edge dislocation density
ρ_s^α	Screw dislocation density
ρ_\perp^α	Edge positive dislocation density
ρ_\top^α	Edge negative dislocation density
ρ_\odot^α	Screw positive dislocation density
ρ_\oplus^α	Screw negative dislocation density
κ^α	Geometrically necessary dislocation (GND) density
τ^α	Resolved shear stress (RSS)
τ_b^α	Back stress
τ_{cr}^α	Slip system resistance
\mathbf{S}_{int}	Total internal stress due to GNDs
f^α	Dislocation flux across the grain boundary
b	Magnitude of Burgers vector
\mathbf{v}^α	Dislocation velocity vector
v_c	Shear wave speed in the material
\mathbf{I}	Second order identity tensor
\times	Cross product
\otimes	Dyadic product
:	Inner product

Table 1: A brief definition of all the significant variables used in the work.

components, respectively, i.e.,

$$\mathbf{F} = \mathbf{F}_e \mathbf{F}_p \quad \text{where } \det \mathbf{F}_e > 0 \quad \text{and} \quad \det \mathbf{F}_p = 1. \quad (3)$$

The elastic part of the deformation gradient \mathbf{F}_e incorporates both lattice rotation and elastic stretch through the relation $\mathbf{F}_e = \mathbf{R}_e \mathbf{U}_e$. The rates of the elastic and plastic components of the deformation gradient are given as

$$\dot{\mathbf{F}}_e = \mathbf{L}\mathbf{F}_e - \mathbf{F}_e\mathbf{L}_p \quad \text{and} \quad \dot{\mathbf{F}}_p = \mathbf{L}_p\mathbf{F}_p. \quad (4)$$

where $\mathbf{L} = \dot{\mathbf{F}}\mathbf{F}^{-1}$ and $\mathbf{L}_p = \dot{\mathbf{F}}_p\mathbf{F}_p^{-1}$. For dislocation-mediated plasticity, the plastic part of the velocity gradient \mathbf{L}_p is expressed in terms of a summation of crystallographic slip rates $\dot{\gamma}^\alpha$ on each slip system α as

$$\mathbf{L}_p = \dot{\mathbf{F}}_p\mathbf{F}_p^{-1} = \sum_{\alpha=1}^{N_{slip}} \dot{\gamma}^\alpha \mathbf{s}_0^\alpha \otimes \mathbf{n}_0^\alpha = \sum_{\alpha=1}^{N_{slip}} \dot{\gamma}^\alpha \mathbf{S}_0^\alpha. \quad (5)$$

The Schmid tensor is expressed as $\mathbf{S}_0^\alpha \stackrel{\text{def}}{=} \mathbf{s}_0^\alpha \otimes \mathbf{n}_0^\alpha$, where \mathbf{s}_0^α and \mathbf{n}_0^α are respectively the slip direction and slip plane normal as defined in the reference configuration. The face centered cubic (fcc) crystal structure has four slip planes that are represented by slip plane normals \mathbf{n}_0^α , with each slip plane having three slip directions represented by \mathbf{s}_0^α . N_{slip} is the total number of slip systems which is 12 for fcc materials.

The stress-strain relation is expressed in an elastically undeformed reference configuration, in terms of the second Piola-Kirchhoff stress $\hat{\mathbf{S}}$ and the elastic Green-Lagrange strain \mathbf{E}_e ,

$$\hat{\mathbf{S}} = \mathbb{C} : \mathbf{E}_e, \quad (6)$$

where \mathbb{C} is a fourth-order anisotropic elasticity tensor in the material symmetry coordinates. The second Piola-Kirchhoff stress $\hat{\mathbf{S}}$ and the elastic component of the Green-Lagrange strain tensor \mathbf{E}_e are respectively defined as,

$$\hat{\mathbf{S}} \equiv \det(\mathbf{F}_e)\mathbf{F}_e^{-1}\sigma\mathbf{F}_e^{-T} \text{ and } \mathbf{E}_e \equiv \frac{1}{2} (\mathbf{F}_e^T\mathbf{F}_e - \mathbf{I}) \quad (7)$$

where \mathbf{I} is the 2nd order identity tensor and σ is the Cauchy stress tensor.

2.1.2 Crystal plasticity material model

For dislocation density-based crystal plasticity material models, the crystallographic slip rate $\dot{\gamma}^\alpha$ is calculated from Orowan's equation [20], and can be written as

$$\dot{\gamma}^\alpha = \rho_m^\alpha b v^\alpha \quad (8)$$

where ρ_m^α and v^α are the mobile dislocation density and dislocation velocity on slip system α , respectively, and b is the magnitude of the Burgers vector. Following [21], the positive and negative character of edge and screw dislocations are tracked as separate dislocation density field variables. Hence, ρ_m^α has contributions from both positive and negative edge and screw dislocations, i.e.,

$$\rho_m^\alpha = \rho_{m,\perp}^\alpha + \rho_{m,\top}^\alpha + \rho_{m,\odot}^\alpha + \rho_{m,\oplus}^\alpha \quad (9)$$

where $\rho_{m,\perp}^\alpha$, $\rho_{m,\top}^\alpha$, $\rho_{m,\odot}^\alpha$ and $\rho_{m,\oplus}^\alpha$ are edge-positive, edge-negative, screw-positive and screw-negative mobile dislocation density, respectively. Thus, the total mobile edge dislocation density can be expressed as $\rho_{m,e}^\alpha = \rho_{m,\perp}^\alpha + \rho_{m,\top}^\alpha$ and similarly for screw dislocations $\rho_{m,s}^\alpha = \rho_{m,\odot}^\alpha + \rho_{m,\oplus}^\alpha$. To model the local evolution of the dislocation densities, the substructure evolution of dislocations are separated based on well-known mechanisms of dislocation network evolution. The three key mechanisms are identified as: (i) multiplication of mobile dislocations, (ii) trapping of mobile dislocations rendering

them immobile [22] and (iii) annihilation of dislocations through interaction with dislocations of the opposite polarity. The evolution of mobile and immobile dislocation takes the form [9],

$$\dot{\rho}_m^\alpha = \dot{\rho}_{\text{mult}}^\alpha - \dot{\rho}_{\text{trap}}^\alpha - \dot{\rho}_{\text{m-ann}}^\alpha \quad (10)$$

$$\dot{\rho}_{im}^\alpha = \dot{\rho}_{\text{trap}}^\alpha - \dot{\rho}_{\text{im-ann}}^\alpha \quad (11)$$

where the subscripts mul, trap and ann stands for multiplication, trapping and annihilation, respectively. In the present study, the terms related to nucleation and recovery are omitted. The other terms in the evolution equations 10 and 11 are expressed as

$$\dot{\rho}_{\text{multi}}^\alpha = \frac{c_{\text{mult}}}{b^2} |\dot{\gamma}_p^\alpha| \quad (12a)$$

$$\dot{\rho}_{\text{trap}}^\alpha = \frac{c_{\text{trap}}}{b} \sqrt{\rho_f^\alpha} |\dot{\gamma}_p^\alpha| \quad (12b)$$

$$\dot{\rho}_{\text{m-ann}}^\alpha = c_{\text{m-ann}} \rho_m^\alpha |\dot{\gamma}_p^\alpha| \quad (12c)$$

$$\dot{\rho}_{\text{im-ann}}^\alpha = c_{\text{im-ann}} \rho_{im}^\alpha |\dot{\gamma}_p^\alpha| \quad (12d)$$

where c_{multi} , c_{trap} , $c_{\text{m-ann}}$ and $c_{\text{im-ann}}$ are material parameters. ρ_f^α is the forest dislocation density on the α^{th} slip system. ρ_f^α is computed from the total dislocation density by projecting the density onto slip system α , and can be expressed as,

$$\rho_f^\alpha = \sum_{\beta=1}^{N_{\text{slip}}} A_f^{\alpha\beta} \rho^\beta \quad \text{where} \quad A_f^{\alpha\beta} = \frac{1}{2} |\mathbf{n}^\alpha \cdot \mathbf{s}^\beta| + \frac{1}{2} |\mathbf{n}^\alpha \cdot (\mathbf{n}^\beta) \times \mathbf{s}^\beta|. \quad (13)$$

The geometrically necessary dislocation (GND) [23, 20, 24] densities for edge and screw populations active on the α^{th} slip system are expressed as,

$$\kappa_e^\alpha = \rho_{m,\perp}^\alpha - \rho_{m,\top}^\alpha \quad (14a)$$

$$\kappa_s^\alpha = \rho_{m,\odot}^\alpha - \rho_{m,\oplus}^\alpha, \quad (14b)$$

From equations 5 and 8 the evolution of the plastic deformation can be written using the Orowan relation,

$$\dot{\mathbf{F}}_p \mathbf{F}_p^{-1} = \sum_{\alpha=1}^{N_{\text{slip}}} b^\alpha (\rho_e^\alpha v_e^\alpha + \rho_s^\alpha v_s^\alpha) \mathbf{s}_0^\alpha \otimes \mathbf{n}_0^\alpha \quad (15)$$

where v_e^α and v_s^α are the signed scalar velocity of edge and screw dislocation densities, respectively, on slip system α .

In general, the dislocation velocity can be expressed as,

$$v^\alpha = \hat{v}(\tau^\alpha, \rho^\beta, T), \quad (16)$$

where τ^α is the resolved shear stress (RSS) on slip system α . The mean velocity of gliding dislocations is expressed as [25, 10],

$$v^\alpha = \frac{\bar{L}^\alpha}{t_w + t_r} \text{sign}(\tau^\alpha - \tau_b^\alpha), \quad (17)$$

where \bar{L}^α is the mean spacing between obstacles, t_w is the wait time that a dislocation spends at an obstacle waiting to overcome it, and t_r is the run time for a dislocation to freely glide between two obstacles. In the present study the main obstacle for the movement of a dislocation is another (forest) dislocation, thus, \bar{L}^α is simply approximated as $\bar{L}^\alpha = 1/\sqrt{\rho^\alpha}$, where ρ^α is the total dislocation density on slip system α .

The waiting time, t_w , for a dislocation to overcome an obstacle characterizes a process which is both stress driven as well as thermally activated and can be expressed as [25, 10, 26],

$$t_w = \frac{1}{\omega} \left(\exp \left[\frac{\Delta G(\tau)}{KT} \right] \right), \quad (18)$$

where ω is the attempt frequency, and K is the Boltzman constant. ΔG is the stress-assisted activation energy and is expressed as,

$$\Delta G^\alpha(\tau) = \Delta G_0 \left\langle 1 - \left(\frac{|\tau^\alpha - \tau_b^\alpha|}{\tau_{cr}^\alpha} \right)^{q_1} \right\rangle^{q_2}, \quad (19)$$

where $\langle x \rangle = 1/2(|x| + x)$, ΔG_0 is the thermal activation constant computed as $\Delta G_0 = g_0 \mu b^3$, τ_b^α is the GND induced back stress and τ_{cr}^α is the slip resistance on slip system α . The exponents q_1 and q_2 are material parameters. The slip resistance, τ_{cr}^α , due to the interaction between a glide dislocation and other dislocations, is expressed in Taylor hardening form as

$$\tau_{cr}^\alpha = \tau_0 + c_1 \mu b \sqrt{\sum_\beta H_{\alpha\beta} (\rho_e^\beta + \rho_s^\beta)}, \quad (20)$$

where τ_0 is the intrinsic resistance to dislocation glide due to lattice friction, c_1 is a material constant and $H_{\alpha\beta}$ is the interaction matrix for hardening [27]. The back stress τ_b^α is computed from the internal stress (\mathbf{S}_{int} , see Section 2.2) as,

$$\tau_b^\alpha = \mathbf{S}_{int} : \mathbf{s}_0^\alpha \otimes \mathbf{n}_0^\alpha. \quad (21)$$

The run time, t_r , is the average free-running time between obstacles and can be expressed as,

$$t_r = \frac{\bar{L}^\alpha}{v_r} \quad (22)$$

where v_r is the running velocity of the dislocation as it glides between two obstacles. The upper limit of free running velocity is restricted to the sound wave speed in that material due to the viscous drag effect. This velocity can be written as [25, 10]

$$v_r^\alpha = c_s (\sqrt{(\xi^\alpha)^2 + 1} - \xi^\alpha), \quad (23)$$

and where ξ^α is expressed as,

$$\xi^\alpha = \frac{B_0(T) c_s}{2b(\tau^\alpha - \tau_b^\alpha)}. \quad (24)$$

2.2 Dislocation Deformation Compatibility (DDC)

The evolution of the mobile dislocation density field has a local contribution associated with dislocation network evolution represented by equation 10, and a non-local contribution resulting from transport. Dislocation transport causes a net-polarity of

the dislocation density field because under an identical effective RSS dislocations of opposite polarity will propagate in opposite directions. This non-zero net-polarity of the dislocation density field leads to the development of an internal stress field associated with long-range elastic interactions of the dislocations via lattice curvature. This internal stress field can either enhance or impede the further movement of dislocations. In DiscoFlux, this internal stress field is approximated as a simple expression related to the gradient of the GND density at a particular material point. There are several related models that similarly approximate this internal stress field in terms of the GND density [28, 29]. Here we use the expression proposed in [10] according to which the internal stress is computed as

$$\tau_{int}^{\alpha} = \frac{\mu b}{2\pi(1-\nu)} L_0^2 \nabla_s \kappa^{\alpha}(z), \quad (25)$$

where τ_{int}^{α} and κ^{α} are the internal stress and GND density, respectively, on slip system α , μ and ν are the effective isotropic shear modulus and Poisson's ratio of the material, and ∇_s is the directional derivative along the slip direction. The total internal stress is computed as the summation of contributions from each individual slip system, i.e.,

$$\mathbf{S}_{int} = \sum_{\alpha=1}^{N_{slip}} \tau_{int}^{\alpha} \mathbf{M}_0^{\alpha}, \quad (26)$$

where \mathbf{M}_0 is expressed as,

$$\mathbf{M}_0 = \frac{1}{2} (\mathbf{s}_0^{\alpha} \otimes \mathbf{n}_0^{\alpha} + \mathbf{n}_0^{\alpha} \otimes \mathbf{s}_0^{\alpha}). \quad (27)$$

2.3 Continuum Dislocation Transport (CDT)

During plastic deformation of crystalline solids, the dislocation mediated plastic deformation occurs due to the movement of dislocations. The associated transport of dislocations occurs both within individual grains and also across GBs.

2.3.1 Intragranular dislocation transport

The local evolution of the dislocations within the grain is modeled using the standard field advection equation. For a conserved scalar quantity, ρ , this can be written as

$$\dot{\rho}^{\alpha} + \nabla_0 \cdot (\rho^{\alpha} \mathbf{v}_c^{\alpha}) = s^{\alpha}, \quad (28)$$

where s^{α} is the source term and \mathbf{v}_c^{α} is the dislocation velocity vector on slip system α . The subscript c in the velocity indicates that the dislocation velocity on slip system α depends on the character of the dislocation and can be expressed as

$$\begin{aligned} \mathbf{v}_{\perp}^{\alpha} &= v_e^{\alpha}(\tau^{\alpha}, \rho_c^{\beta}, T) \mathbf{s}_0^{\alpha} \\ \mathbf{v}_{\top}^{\alpha} &= -v_e^{\alpha}(\tau^{\alpha}, \rho_c^{\beta}, T) \mathbf{s}_0^{\alpha} \\ \mathbf{v}_{\odot}^{\alpha} &= v_s^{\alpha}(\tau^{\alpha}, \rho_c^{\beta}, T) \mathbf{s}_0^{\alpha} \times \mathbf{n}_0^{\alpha} \\ \mathbf{v}_{\oplus}^{\alpha} &= -v_s^{\alpha}(\tau^{\alpha}, \rho_c^{\beta}, T) \mathbf{s}_0^{\alpha} \times \mathbf{n}_0^{\alpha}. \end{aligned} \quad (29)$$

2.3.2 Intergranular dislocation transport

It is generally well understood, and has been directly observed [3, 4], that GBs in a polycrystalline material are a barrier to the free movement of dislocations. Consequently, dislocations typically accumulate or pile-up at GBs during plastic deformation processes. However, many GBs allow finite (non-zero) slip transfer across the interface, effectively enabling some dislocation movement across the GBs. The permeability of dislocations across a GB depends on several different factors related to the GB character and the adjacent material state variables (e.g. stress, dislocation density). There are two main types of criterion that have been used to determine the probability of transfer of dislocation across a GB: geometric criterion [30] and energetic criterion [31]. A detailed review of these approaches can be found in [32, 3, 33]. In the present work, we focus on geometry based criterion, recognizing that the framework will permit future extension to models that capture the evolving description of the GB character in the context of energy and other state descriptors. Another rationale behind this choice is that different combinations of multiple geometric features of the GB and the adjacent grains can give rise to a similar GB energy but very different transmission behavior. The reason behind this is that GB energy can be characterized using coincident site lattice (CSL). But the CSL Σ value does not represent a full description of GB which has five degrees of freedom [31].

Figure 1 shows a typical arrangement of a GB with the relevant geometric features and a single pair of slip systems from the adjacent grains [32]. In the geometry based

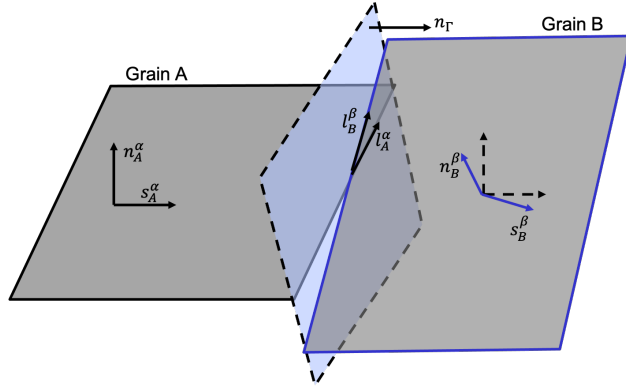


Figure 1: A schematic representation of the relevant geometric features used within the dislocation flux transfer criteria in this work following [32]. Slip plane normal, \mathbf{n}^α , and direction, \mathbf{s}^α , for a particular pair of slip systems α and β in adjacent Grains A and B, respectively, and the GB interface normal direction, \mathbf{n}_Γ , are denoted. The intersection of the slip planes and the GB surface are indicated by the vectors \mathbf{l}_A^α and \mathbf{l}_B^β .

criterion, geometric features of the GB and grains, e.g. slip directions $\mathbf{s}_A^\alpha, \mathbf{s}_B^\beta$, slip plane normals $\mathbf{n}_A^\alpha, \mathbf{n}_B^\beta$, and the GB plane normal \mathbf{n}_Γ , are used to construct the criterion. Here Grains A and B represent the two grains that are involved in the formation of the GB with the unit normal \mathbf{n}_Γ . There are several geometric criteria that have been developed in the past to model the dislocation transfer across a GB [34, 33, 35, 36]. In [34] the

interaction matrix is defined as

$$N_{\alpha\beta} = (\mathbf{n}_A^\alpha \cdot \mathbf{n}_B^\beta)(\mathbf{s}_A^\alpha \cdot \mathbf{s}_B^\beta) + (\mathbf{n}_A^\alpha \cdot \mathbf{s}_B^\beta)(\mathbf{s}_A^\alpha \cdot \mathbf{n}_B^\beta). \quad (30)$$

The interaction matrix $N_{\alpha\beta}$ is an $N_{\text{slip}} \times N_{\text{slip}}$ matrix, where N_{slip} is the number of slip systems in the material. This geometric criterion assumes that the local stress developed in the adjacent grain due to the pile-up of dislocations in the neighboring grain is purely shear in nature. According to this criterion, the geometric alignment between two slip systems from the adjacent grains are the only factor that impacts the transfer of slip across the GB. The above criterion is slightly modified by dropping the second term and used in collaboration with the Schmid factor and stress concentration ahead of the pile-up [33] to determine the outgoing slip system when a dislocation transmits across a GB. None of the above criterion consider any features of the GB plane itself e.g, the GB plane normal. Atomic scale study showed that the angle between the lines of intersection of GB plane with incoming and outgoing slip plane plays an important role in the mechanism of slip transfer at the GB [37, 38]. Conversely, other criteria have been proposed that do incorporate some of the GB features, such as that developed in [35, 36],

$$M_{\alpha\beta} = (\mathbf{l}_A^\alpha \cdot \mathbf{l}_B^\beta)(\mathbf{s}_A^\alpha \cdot \mathbf{s}_B^\beta), \quad (31)$$

where \mathbf{l}_A^α is the line of intersection between the GB plane and slip plane α of Grain A and is defined as $\mathbf{l}_A^\alpha = (\mathbf{n}_A^\alpha \times \mathbf{n}_\Gamma)/|\mathbf{n}_A^\alpha \times \mathbf{n}_\Gamma|$. \mathbf{n}_Γ is the unit normal to the GB between Grain A and Grain B and pointing away from Grain A. This criterion is used to determine the slip plane of the outgoing dislocation density and a separate stress criterion is used to determine the slip direction within that slip plane. Figure 2(a) shows the interaction matrix calculated using equation 31 for slip transmission of 12 possible fcc slip systems for a bi-crystal in which both grains are aligned (i.e. zero misorientation). The slip plane normal and slip direction corresponding to the slip system index are given in Table 3 of Appendix A. For this case, in which the two grains are perfectly aligned, each of the slip systems in both grains are also perfectly aligned with their corresponding system. Thus, it is expected that dislocations should continue gliding precisely along the same slip system after crossing the GB. However, it can be seen from Figure 2(a) that this particular interaction matrix (equation 31) fails to provide an unique direction of slip transfer. Specifically, ideal slip transfer is indicated for four cases off the diagonal of the matrix. Therefore, we propose a new criterion which fulfills this basic requirement in the limit of perfect alignment and is defined as

$$M_{\alpha\beta}^{\text{mod}} = |(\mathbf{l}_A^\alpha \cdot \mathbf{l}_B^\beta)(\mathbf{s}_A^\alpha \cdot \mathbf{s}_B^\beta)|(\mathbf{n}_A^\alpha \cdot \mathbf{n}_B^\beta). \quad (32)$$

This criterion incorporates the geometric features of slip systems in the both grains comprising the GB as well as geometric features of the GB itself. For dislocations accumulated on α 'th slip system of Grain A at the GB, the index of the corresponding outgoing dislocations are determined by investigating the maximum absolute value of $M_{\alpha\beta}^{\text{mod}}$ along the α 'th row of the interaction matrix. It can be seen from equation 32 that the range of the interaction matrix is $(-1, 1)$. The sign of $M_{\alpha\beta}^{\text{mod}}$ is determined by slip plane normals \mathbf{n}_A^α and \mathbf{n}_B^β only. Hence, negative magnitude signifies that the dislocation transfer happens between dislocation densities of opposite sign, e.g., when

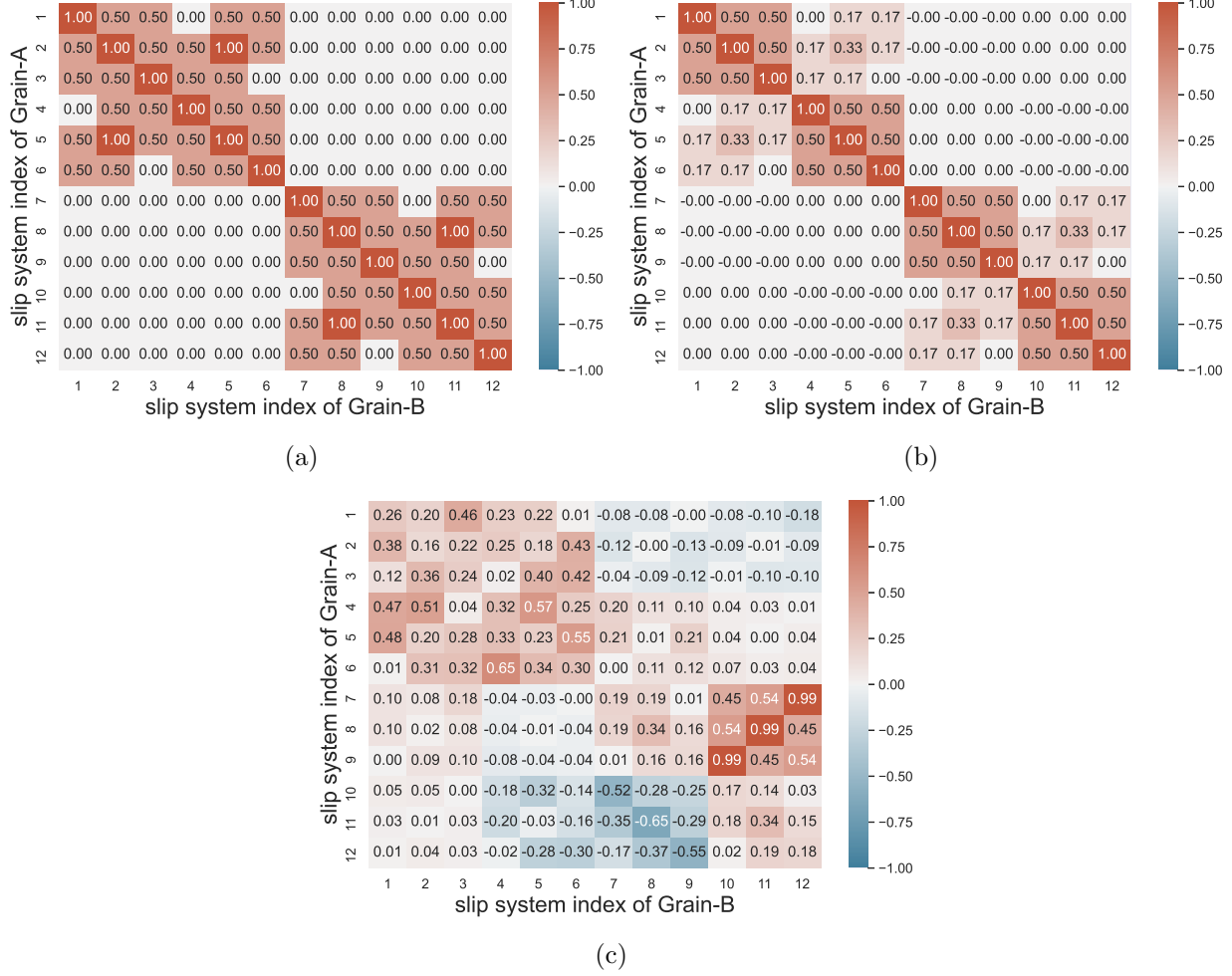


Figure 2: Interaction matrix for transfer of dislocations across a GB based on (a) criterion equation 31 with misorientation angle of 0°, (b) criterion equation 32 with misorientation angle of 0°, (c) criterion equation 32 with misorientation angle of 50°. Statistical data visualization tool Seaborn [39] is used to plot these data as heat-map.

the misorientation between the slip systems of incoming and outgoing dislocation approaches 180°, it is possible that positive dislocations from the incoming slip system will get transferred to the outgoing slip system as negative dislocation and vice versa.

Figures 2(b) and (c) show coefficient values in the new interaction matrix, $M_{\alpha\beta}^{\text{mod}}$, calculated with equation 32 for two different grain misorientations. Similar to Figure 2(a) for the interaction matrix of equation 31, Figure 2(b) highlights the case of zero misorientation between the two grains. Figure 2(c) presents a new interaction matrix for a bi-crystal with Euler angles of (30,-20,0) for Grain A and (-20,30,0) for Grain B respectively according to Bunge convention [40]. With this revised geometric criterion, for zero misorientation, Figure 2(b) now shows what one would expect for the case in which all slip systems are perfectly aligned. Thus, in the cube-on-cube orientation case, it is now a unique solution that dislocations will continue to glide in the same outgoing

slip system as incoming slip system. When there is finite misorientation e.g, Figure 2(c), the interaction matrix can have the largest value for each row in an off-diagonal position. The interaction matrix with off-diagonal dominant terms signifies that slip system index of the incoming dislocations ('in') is different than that of the outgoing dislocations ('out'). For example, if we explore row-1 of Figure 2(c) we can conclude that if there is an accumulation of dislocation density at the GB on slip system-1 of Grain A, the interaction shows a maximum value, indicating probable transmission, with slip system-3 of Grain B. Section 3.2 discusses the transmission of dislocation density across grains with this same misorientation in more detail. In the present work, for each slip system of the incoming dislocations there will be exactly one slip system for outgoing dislocation, which is determined by the maximum value provided by equation 32. However, Figure 2(c) clearly shows that in many cases the maximum value in the interaction matrix for any given slip system may not be close to ± 1 , and in some case there are several similar and relatively large values. For example, slip system-4 of Grain A has a maximum value of 0.57 indicating transmission onto slip system-5 of Grain B. However, there are values of 0.47 and 0.51 indicating that slip systems 1st and 2nd of Grain B may also be oriented favorably for transmission of at least some part of the fluxing dislocation density on slip system-4 of Grain A. Addressing slip transfer of dislocation density from one to many slip systems based on the critical value of the components of the interaction matrix is subject of future study.

Once the direction of slip transfer from incoming ('in') dislocations to outgoing ('out') dislocations at the GB is identified, the transferred flux at the GB from slip system α of Grain A to β of Grain B is expressed as,

$$f_{G_B(\text{in})}^{\beta} = f_{G_A(\text{out})}^{\alpha} = \begin{cases} \rho_{G_A}^{\alpha} \mathbf{v}_{G_A}^{\alpha} \cdot \mathbf{n}_{\Gamma} & \text{when } \begin{cases} \rho_{G_A}^{\alpha} > \rho_{\text{crt}} \\ \tau_{G_A}^{\alpha} > \tau_{\text{crt}} \end{cases} \\ 0 & \text{otherwise} \end{cases} \quad (33)$$

where $\rho_{G_A}^{\alpha}$, $\mathbf{v}_{G_A}^{\alpha}$ are dislocation density and velocity vector respectively for α slip system of Grain A. ρ_{crt} represents the critical dislocation density beyond which dislocation transfer across the GB happens. This can be related to the physical mechanism of dislocation pile up at the GB that facilitates the dislocation transfer across the GB [41, 42, 33, 3]. ρ_{crt} assumes the magnitude of the initial dislocation density when there is no misorientation between two grains. Also at zero misorientation, the interaction matrix becomes diagonal and the maximum magnitude at the diagonal becomes 1.00. Hence the following linear form of ρ_{crt} is used in the present study,

$$\rho_{\text{crt}} = \rho_0 + (\rho_{\text{crt}}^* - \rho_0) \left(1 - \max \left[M_{\alpha\beta}^{\text{mod}} : \beta = 1, N_{\text{slip}} \right] \right) \quad (34)$$

ρ_{crt}^* and τ_{crt} are material parameters. For each slip system in Grain A (α), the corresponding β slip system in Grain B is determined from the interaction matrix. It should also be noted that the slip transfer across the GB occurs only when $\mathbf{v}_{G_1}^{\alpha} \cdot \mathbf{n}_{G_A-G_B}$ assumes a positive value.

2.4 Numerical implementation of the model into MOOSE

The main equation that need to be time integrated within the crystal plasticity model is equation 4. During the time increment from (t) to (t+ Δt) the updated \mathbf{F}_p can be

expressed as:

$$\mathbf{F}_p(t + \Delta t) = \left(\mathbb{I} + \sum_{\alpha=1}^{N_s} \Delta t \dot{\gamma}^\alpha \mathbf{s}_0^\alpha \otimes \mathbf{n}_0^\alpha \right) \mathbf{F}^p(t). \quad (35)$$

With this updated $\mathbf{F}_p(t + \Delta t)$, the incremented second Piola-Kirchhoff stress can be written as,

$$\begin{aligned} \mathbf{S}(t + \Delta t) &= \mathbb{C} : \mathbf{E}_e(t + \Delta t) \\ &= \frac{1}{2} \mathbb{C} : (\mathbf{F}_e^T(t + \Delta t) \mathbf{F}_e(t + \Delta t) - \mathbf{I}) \\ &= \frac{1}{2} \mathbb{C} : (\mathbf{F}_p^{-T}(t + \Delta t) \mathbf{F}^T(t + \Delta t) \mathbf{F}(t + \Delta t) \mathbf{F}_p^{-1}(t + \Delta t) - \mathbf{I}) \\ &\approx \frac{1}{2} \mathbb{C} : [\mathbf{A}(t + \Delta t) - \mathbb{I}] - \sum_{\alpha} \Delta t \dot{\gamma}(\mathbf{S}(t + \Delta t), \tau_b^\alpha(t + \Delta t), \tau_{cr}^\alpha(t + \Delta t)) \mathbf{B}^\alpha \end{aligned} \quad (36)$$

where

$$\begin{aligned} \mathbf{A}(t + \Delta t) &\stackrel{\text{def}}{=} \mathbf{F}^{p-T}(t) \mathbf{F}^T(t + \Delta t) \mathbf{F}(t + \Delta t) \mathbf{F}^{p-1}(t) \\ \mathbf{B}^\alpha &\stackrel{\text{def}}{=} \frac{1}{2} \mathbb{C} : [\mathbf{A}(t + \Delta t) \mathbf{S}_0^\alpha + \mathbf{S}_0^{\alpha T} \mathbf{A}(t + \Delta t)] \end{aligned} \quad (37)$$

The nonlinear equation 36 is solved iteratively using a Newton-Raphson solver for the second Piola-Kirchhoff stress. The i 'th iteration can be written as,

$$\mathbf{S}^{i+1}(t + \Delta t) = \mathbf{S}^i(t + \Delta t) - \mathbb{J}_{\text{stress}}^{-1} : \mathbb{R}_{\text{stress}}^i \quad (38)$$

where $\mathbb{R}_{\text{stress}}$ is the residual and $\mathbb{J}_{\text{stress}}$ is the Jacobian. The residual $\mathbb{R}_{\text{stress}}$ is computed on the second Piola-Kirchhoff stress and can be expressed as,

$$\mathbb{R}_{\text{stress}}^i = \mathbf{S}^i(t + \Delta t) - \mathbb{C} : \mathbf{E}_e(t + \Delta t) \quad (39)$$

Thus the Jacobian becomes,

$$\mathbb{J}_{\text{stress}} = \frac{\partial \mathbb{R}_{\text{stress}}^i}{\partial \mathbf{S}^i} = \mathbb{I} - \left[\mathbb{C} : \frac{\partial \mathbf{E}_e}{\partial \mathbf{F}_e} \frac{\partial \mathbf{F}_e}{\partial \mathbf{F}_p^{-1}} \frac{\partial \mathbf{F}_p^{-1}}{\partial \mathbf{S}} \right] \quad (40)$$

Figure 3 shows the flowchart for the stress update loop.

For numerical implementation of the dislocation transport, the equation 28 is converted to weak form. The corresponding residual can be written as

$$\begin{aligned} \mathbb{R}_{\text{CDT}}^i &= \int_{V_0} (\dot{\rho} + \nabla_0 \cdot (\rho \mathbf{v}_c) - s) \psi_i dV \\ &= \int_{V_0} \dot{\rho} \psi_i dV + \int_{V_0} \nabla_0 \cdot (\rho \mathbf{v}_c) \psi_i dV - \int_{V_0} s \psi_i dV \\ &= \int_{V_0} \dot{\rho} \psi_i dV - \int_{V_0} \rho \nabla_0 \psi_i \cdot \mathbf{v}_c dV + \oint_{\Omega_0} \rho \psi_i \mathbf{v}_c \cdot \mathbf{n} d\Omega - \int_{V_0} s \psi_i dV \\ \mathbb{R}_{\text{CDT}}^i &= \left(\psi_i, \frac{\partial \rho_h}{\partial t} \right) - (\nabla_0 \psi_i, \mathbf{v} \rho) + \langle \psi_i, \rho \mathbf{v} \cdot \mathbf{n} \rangle - (\psi_i s) \end{aligned} \quad (41)$$

where ψ_i is the test function and ρ_h is the trial solution. The terms within curved bracket (\bullet) are volume integrated and terms within the angular bracket (\bullet) are surface

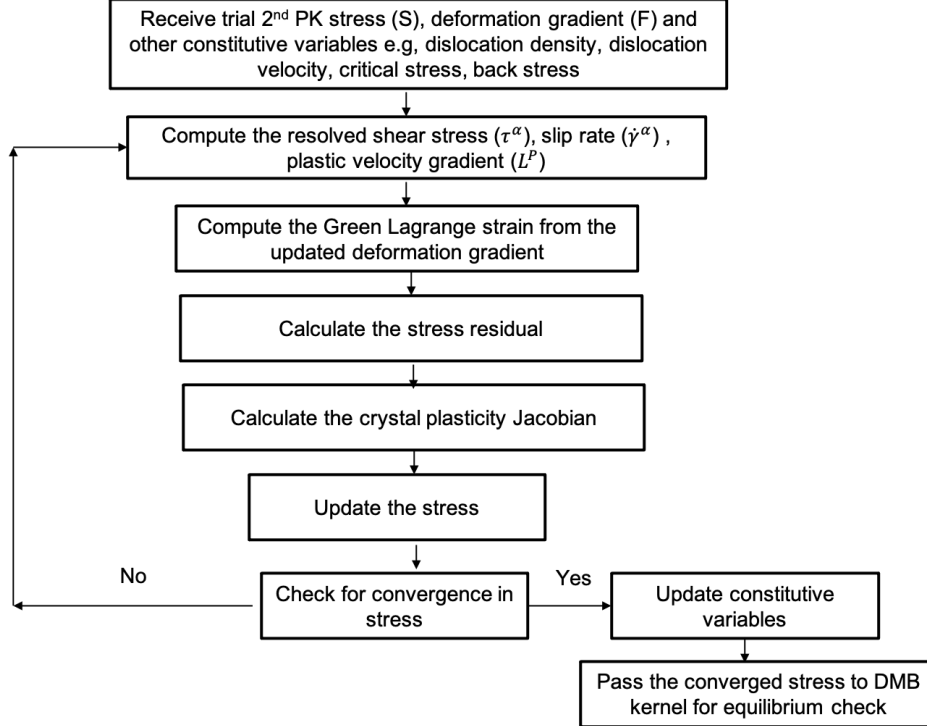


Figure 3: Flow chart for the stress update loop within the DMB module.

integrated. The first and the last term in equation 41 is the residual contribution coming from the time derivative and source term respectively in equation 28. The second and third terms are due to the residual contribution from the advection term. The numerical solution of hyperbolic partial differential equations (PDEs), such as the abovementioned advection equation, are prone to show oscillation in their solution. Some kind of numerical stabilization is needed to eliminate this oscillation. In the present study, to eliminate this spurious oscillation the 'upwind' scheme is used for the stabilization purpose of the advection term [43]. Correction due to the upwind scheme only effects the second term in equation 41. To construct the modified residual, first the upwind and downwind nodes are identified in an element. For this purpose, first we compute the residual contribution from the advection term in equation 41

$$\tilde{\mathbb{R}}_{\text{adv}}^i = -(\nabla_0 \psi_i, \mathbf{v}) \quad (42)$$

if $\tilde{\mathbb{R}}^i > 0$ then it signifies that the corresponding node is an 'upwind' node. The residual of the corresponding node is set to,

$$\mathbb{R}_{\text{adv}}^i = \tilde{\mathbb{R}}_{\text{adv}}^i \rho_i \quad (43)$$

where ρ_i is the dislocation density at node i . Then the total outflow of density from all upwind nodes are computed,

$$M_{\text{out}} = \sum_{\text{upwind nodes}} \tilde{\mathbb{R}}_{\text{adv}}^i \rho_i \quad (44)$$

where M_{out} is the total outflow from the upwind nodes. To conserve the quantity the

residual of the downwind nodes are defined as,

$$\mathbb{R}_{\text{adv}}^i = \tilde{\mathbb{R}}_{\text{adv}}^i M_{\text{out}} / M_{\text{in}} \quad (45)$$

where M_{in} is defined as,

$$M_{\text{in}} = - \sum_{\text{downwind nodes}} \tilde{\mathbb{R}}_{\text{adv}}^i. \quad (46)$$

The second term in equation 41 is evaluated on the boundary Ω . The boundary consists of both the external boundary (Ω_{ext}) and internal boundary or the GB (Ω_{GB}) i.e., $\Omega = \Omega_{\text{ext}} \cup \Omega_{\text{GB}}$. In the present study, two types of boundary conditions are used at the external boundary (Ω_{ext}): a no-flow boundary condition and a free-flow boundary condition. For the no-flow boundary condition the residual condition from the boundary term becomes zero,

$$\mathbb{R}_{\text{BC-ext}}^i = \mathbf{0}. \quad (47)$$

For the free-flow boundary condition the residual contribution becomes,

$$\mathbb{R}_{\text{BC-ext}}^i = \langle \psi_i, \rho \mathbf{v} \cdot \mathbf{n} \rangle. \quad (48)$$

For internal boundaries such as GBs, the residual contribution due to the flux boundary condition becomes,

$$\begin{aligned} \mathbb{R}_{\text{BC-GB+}}^i &= \langle \psi_i, \rho \mathbf{v} \cdot \mathbf{n}_\Gamma \rangle \quad \text{for } \Omega \in \Omega_{\text{GB+}} \\ \mathbb{R}_{\text{BC-GB-}}^i &= -\langle \psi_i, \rho \mathbf{v} \cdot \mathbf{n}_\Gamma \rangle \quad \text{for } \Omega \in \Omega_{\text{GB-}} \end{aligned} \quad (49)$$

where $\Omega_{\text{GB+}}$ corresponds to the side of the GB that dislocations are fluxing from, and $\Omega_{\text{GB-}}$ is the side of the GB where the dislocations fluxing to.

3 Simulation results and discussion

We applied DiscoFlux with the new GB transport theory implemented into MOOSE [17] to numerical test problems in order to assess the implementation. Specifically, we have developed three problems that compare the simulated deformation response of single crystal, bi-crystal and polycrystal configurations utilizing the new features. In the single crystal problem there is no GBs, and therefore, the GB dislocation flux model is not invoked. Thus, we can test that the DiscoFlux implementation in MOOSE is operational before including the extensions of the model that account for dislocation dentistry flux through GBs. For the bi-crystal and polycrystal problems, dislocation transport both within the grain and across the GB are present.

The material parameters used for all of the simulations are specified in Table 2. These values are largely taken from previous work [10], and those that are not are either material parameters or were simply specified by using reasonable approximations for metals, specifically copper. In other words, the material model parameters were selected to be approximately representative of copper deformation behavior, but we have not performed any detailed calibration to experiments. To keep the model simple, in the present study only edge dislocation are considered. We note that the primary goal of this work is not identification of the optimal parameter set to represent any actual material. Rather we use reasonable parameter values to demonstrate and assess the new features of the model in a systematic way.

Parameter	value	Unit	Reference
ρ_0	1.0×10^5	mm^{-2}	[10]
C_{11}	169.0	GPa	[10]
C_{12}	121.0	GPa	[10]
C_{44}	75.3	GPa	[10]
c_{multi}	8.96×10^{-5}	-	-
c_{trap}	3.0×10^{-3}	-	-
$c_{\text{m-ann}}$	0.5	-	-
$c_{\text{imm-ann}}$	0.5	-	-
ρ_{crt}^*	$2.2\rho_0$	mm^{-2}	-
τ_{crt}	50	MPa	-
ω	8.0×10^{11}	s^{-1}	[10]
τ_0	10	MPa	[10]
c_1	0.25	-	-
q_1	0.33	-	[10]
q_2	1.63	-	[10]
g_0	0.87	-	[10]
b	2.56×10^{-7}	mm	[44]
B_0	3.0×10^{-11}	MPa-s	[10]

Table 2: Numerical values of the material parameters used in this study.

3.1 A single crystal sample under shear loading

DiscoFlux was used to simulate a single crystal under shear loading, and to compute the evolution of several of state variables under these conditions. A rectangular prismatic domain of dimension $100\mu\text{m} \times 100\mu\text{m} \times 50\mu\text{m}$ was used for the simulation, and was discretized into 500 regular eight-noded linear hexahedral elements. The sample was continuously deformed by applying a displacement controlled shear strain ($\dot{\gamma} = 0.1\text{s}^{-1}$) at the top surface as shown in Figure 4(a). The bottom surface was restrained against any displacement. A free flow boundary condition was applied on the left, right, front, and back surfaces of the sample domain to allow for free flux of dislocations across those surfaces. The free-flow boundary condition is imposed by specifying the boundary term in the weak form of dislocation transport equation 41. The flux through the external surface is quantified by equation 48, and whether the flux normal to the surface is inflow or outflow is determined based on the sign of $\mathbf{v} \cdot \mathbf{n}$.

Figure 4(b) compares the evolution of the volume-averaged stress with respect to volume-averaged strain when using the local crystal plasticity model (CP-Local) with that obtained when using DiscoFlux with active dislocation transport (CP-DiscoFlux). The difference between these two models is that CP-Local does not include any non-local evolution of the dislocation density field via the spatial dislocation transport mechanism. For CP-Local, the dislocation density field evolves locally according to equation 12, while for CP-DiscoFlux the dislocation density evolves due to the local evolution (i.e., according to equation 12), as well as due to the physical transport of dislocations as described in section 2.3. As can be seen from the evolution of the stress,

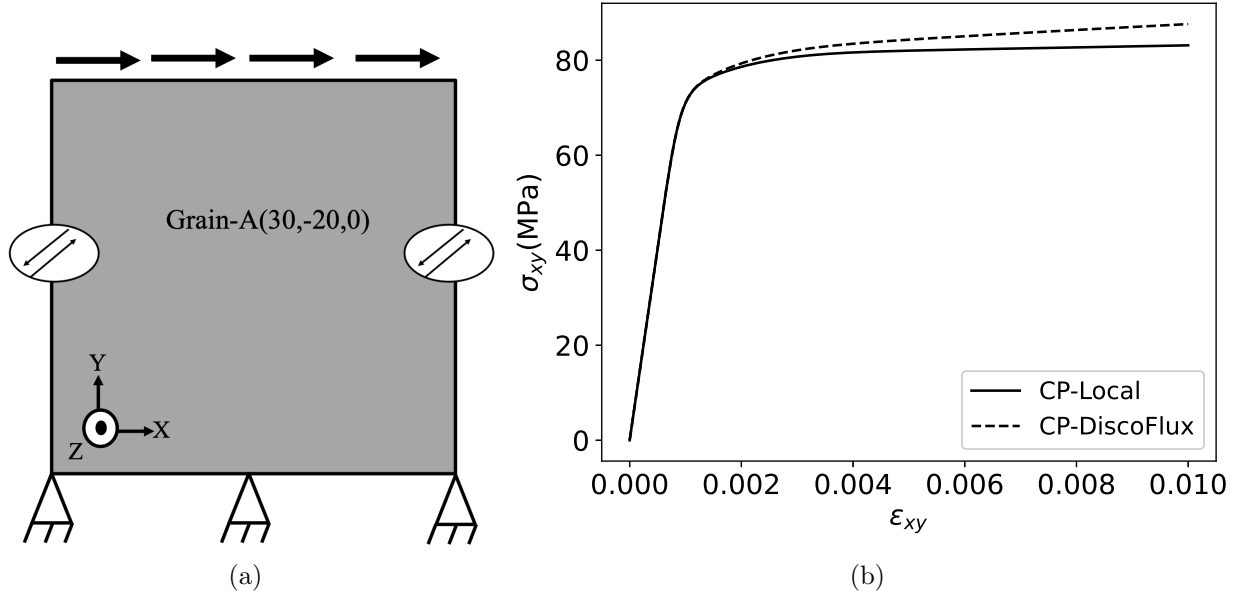


Figure 4: (a) Simulation set-up for single crystal shear test. (b) Evolution of volume averaged stress (σ_{xy}) with respect to volume averaged strain (ϵ_{xy}).

incorporation of dislocation transport (CP-DiscoFlux) within the model leads to the development of GNDs which in turn increases the effective hardening in comparison to that resulting from the CP-Local model.

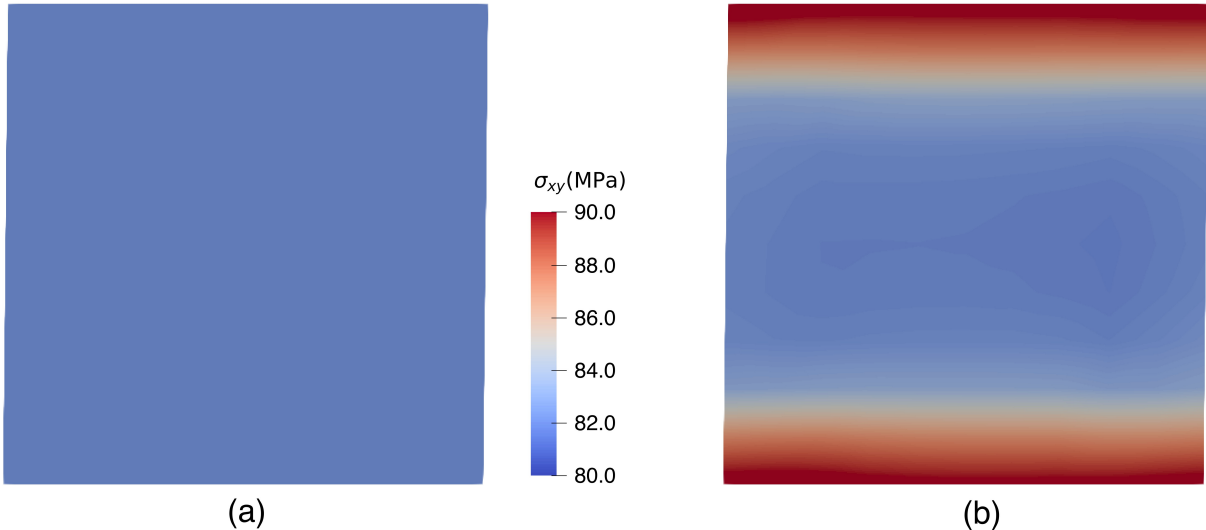


Figure 5: Spatial distribution of the stress (σ_{xy}) under shear loading in a single-crystal using (a) local crystal plasticity model (CP-Local) and (b) DiscoFlux (CP-DiscoFlux). The figure corresponds to a macroscopic volume average strain of $\epsilon_{xy} = 0.01$. Paraview [45] is used to plot the spatial distribution of field variables in this work.

In addition to exhibiting different hardening responses, the different formulations lead to different stress states in the material at the same magnitude of average strain as shown in Figure 5 for $\epsilon_{xy} = 0.01$. The CP-Local model predict a uniform stress distribution, as is expected for this problem. However with CP-DiscoFlux, a heterogeneous stress distribution evolves, producing higher stress states at the top and bottom in comparison to the center of the sample. In CP-DiscoFlux, the evolution of the back stress causes a net dislocation polarity to emerge. This is representative of dislocations moving across the grain and piling up against the impenetrable boundaries, causing high stress regions near these boundaries.

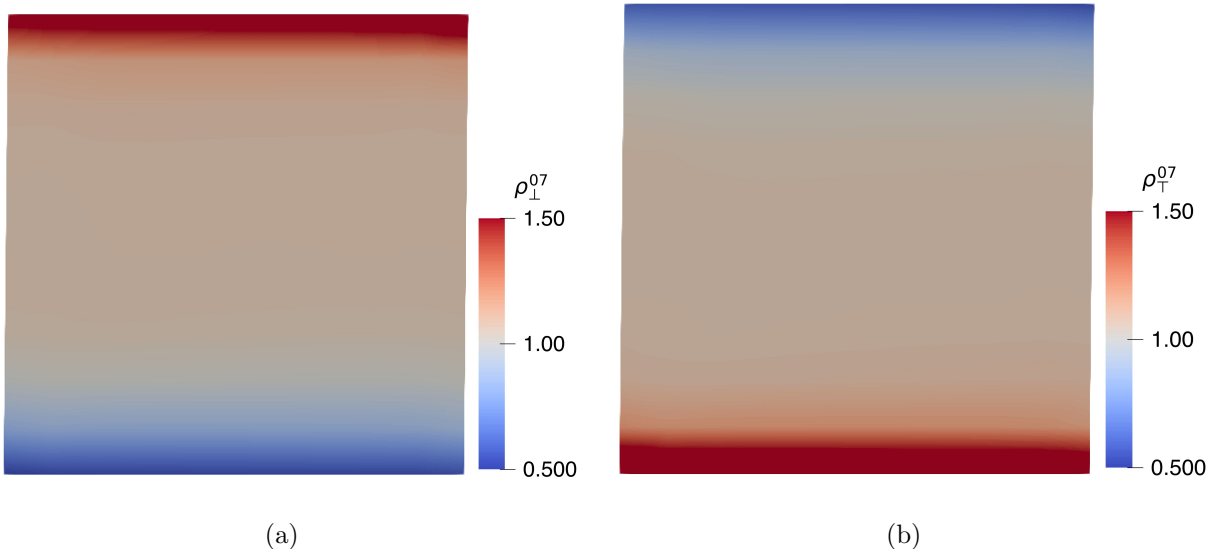


Figure 6: Field distribution of the edge dislocation density (a) ρ_{\perp}^{07} and (b) ρ_{\parallel}^{07} on slip system 7 under shear loading in a single crystal using the ‘DiscoFlux’ model. The magnitude of the dislocation density is normalized by the initial dislocation density, $\rho_0 = 1.0 \times 10^6 \text{ mm}^{-2}$.

Dislocations of opposite character glide in opposite directions (see equation 29). Figure 6 shows one such distribution for the edge dislocation density on slip system 7 at a macroscopic strain of $\epsilon_{xy} = 0.01$. Dislocations of positive character have moved towards the top of the domain (Figure 6(a)), while dislocations of negative character have moved in the opposite direction (Figure 6(b)). This leads to piling up of positive edge dislocation towards the top and depletion towards the bottom of the specimen. An opposite trend is observed for negative edge dislocation. This effective segregation of the dislocation field is also reported in Discrete Dislocation Dynamics (DDD) simulations [46].

The net dislocation polarity is a measure of the GND density in the material. The corresponding spatial distribution of GND density for edge dislocations on the slip system 7 is shown in Figure 7(a). The presence of GNDs gives rise to the internal stress that is quantified in the form of a back stress, which is proportional to gradients of κ_e^α . The associated back stress field within the material is shown in Figure 7(b). We note that owing to the free flow boundary condition for dislocation transport on the left, right, front, and back there is no accumulation or depletion of dislocation

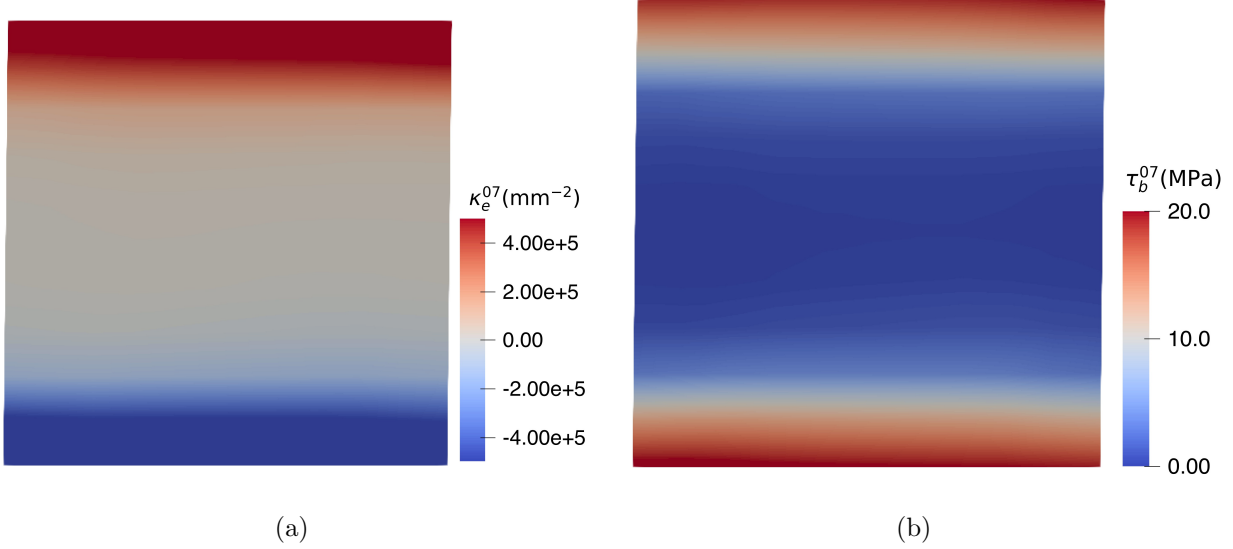


Figure 7: Spatial distribution of (a) GND density κ_e^{07} and (b) back stress τ_b^{07} on slip system 7 under shear loading in a single crystal using DiscoFlux.

density along these boundaries. Because this test problem comprises a single crystal, the domain does not include any GB interfaces and therefore the dislocation density flux discussed in section 2.3.2 is inactive.

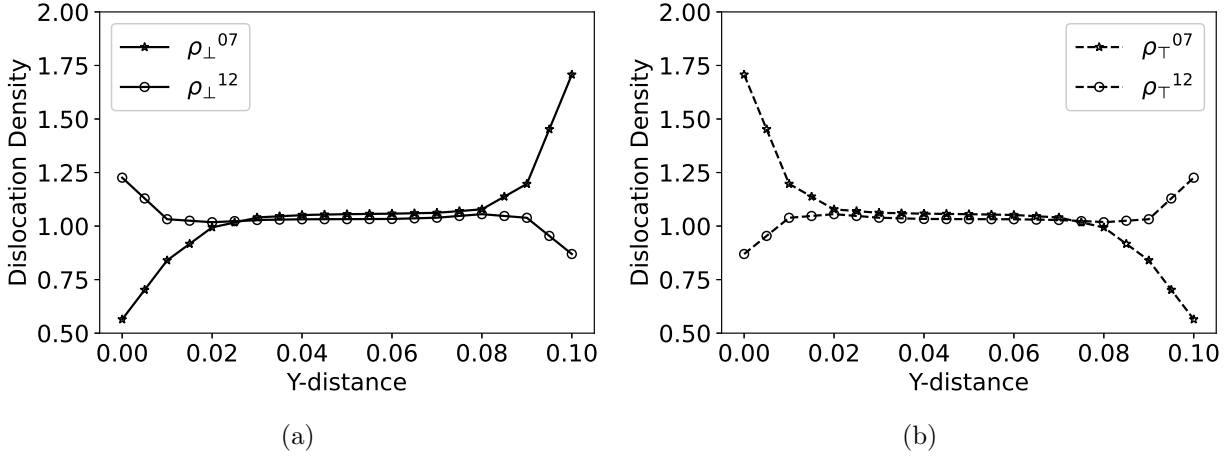


Figure 8: Distribution of dislocation density on 7th and 12th slip-system along the vertical line through the center of the specimen, (a) positive edge (\perp) dislocation density (b) negative edge (\top) dislocation density.

Figure 8 shows the distribution of edge dislocation density along a vertical line through the center of the specimen. Based on the crystal orientation and loading, among twelve slip systems only 7th and 12th are active. The distribution of positive edge dislocation density on the 7th and 12th slip systems are shown in Figure 8(a) and the corresponding distribution for the negative edge dislocation density on these systems is shown in Figure 8(b). It can be seen from Figure 8 that the accumulation

trend of dislocation density of opposite character is also opposite as seen in Figure 6. Also the dislocation accumulation trend on 7th and 12th slip systems are opposite because of the relative orientation of the slip direction and the sign of the RSS on that slip system.

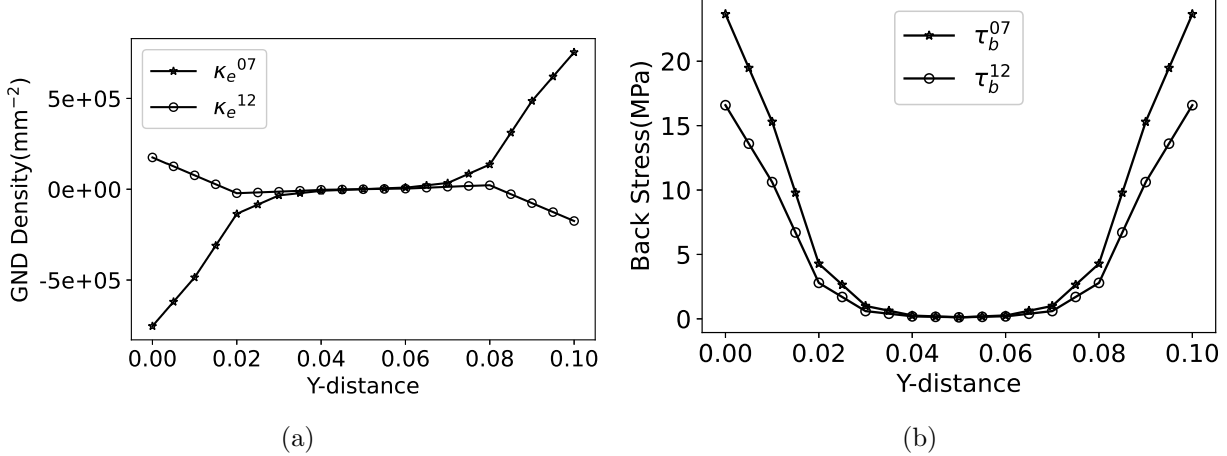


Figure 9: Distribution of (a) GND density and (b) back stress on the 7th and 12th slip systems along a vertical line through the center of the specimen.

Segregation of dislocations of opposite sign leads to the development of net no-zero polarity in dislocation density which is characterized as GND density. Figure 9(a) shows the distribution of GND density along the same vertical line through the center of the specimen. Due to the no-flow boundary condition for dislocation density at the top and bottom of the specimen, the GND density is maximum in the region near top and bottom. The relative difference in the GND density between slip systems 7 and 12 is due to their different orientation, which results in a different RSS on each system and thus, different dislocation velocities. The corresponding distribution of back stress is shown in Figure 9(b). Large GND densities near the top and bottom of the specimen boundary lead to the development of large internal stress, which in turn contributes to the development of large back stress near these boundaries.

3.2 A bi-crystal sample under compressive loading

In this section we analyse the results for simulations of a bi-crystal test problem under various model assumptions. Figure 10(a) shows the problem set-up for the bi-crystal. The overall dimensions of the rectangular prismatic sample are $100\mu\text{m} \times 100\mu\text{m} \times 50\mu\text{m}$. The domain is split equally along y-axis to create two grains. The orientation of the bottom grain (Grain A) and the top grain (Grain B) are $(30^\circ, -20^\circ, 0^\circ)$ and $(-20^\circ, 30^\circ, 0^\circ)$ respectively, based on the Bunge [40] rotation convention. The choice of this particular orientation is arbitrary. Similar to the previous case shown for a single crystal, a fixed and roller displacement boundary condition is applied to the bottom surface of the specimen, and the top surface is deformed at constant compressive strain rate of $\dot{\epsilon} = 0.1\text{s}^{-1}$. The whole domain is discretized using 500 regular eight-node hexahedral elements. A free flow boundary condition for dislocation density is applied at the left, right, front and back surfaces.

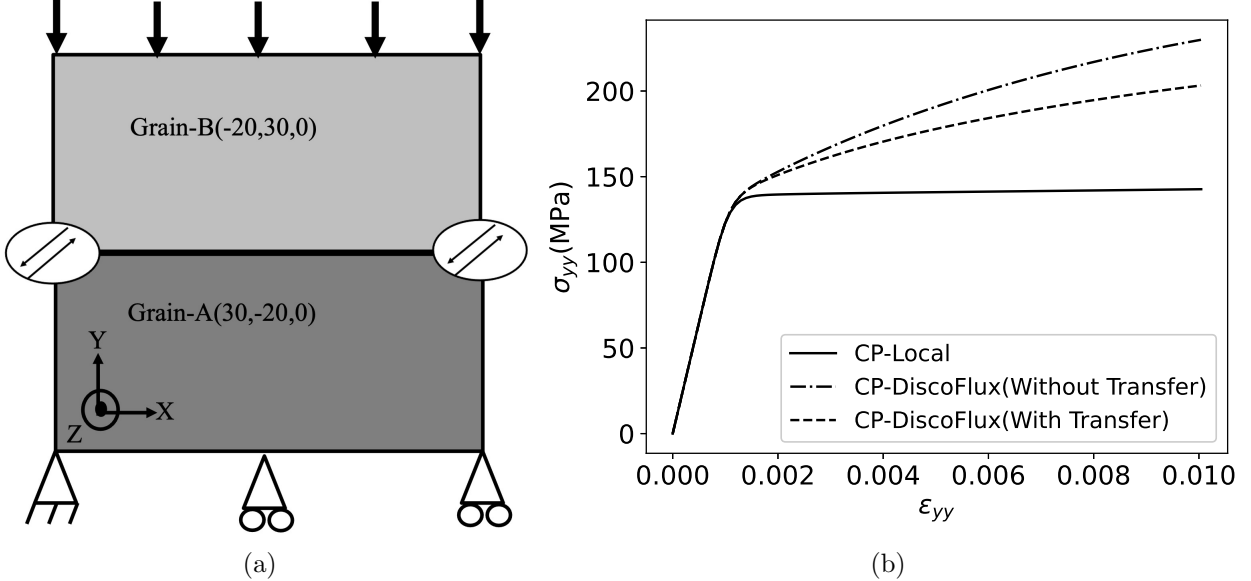


Figure 10: (a) Simulation set-up for a bi-crystal under compressive loading. (b) Evolution of the volume averaged stress (σ_{yy}) with respect to the volume averaged strain (ϵ_{yy}).

Figure 10(b) shows the volume averaged stress-strain response of the specimen for CP-Local and two cases of CP-DiscoFlux that exclude and include the transfer of dislocations across the GB, labeled as CP-DiscoFlux(Without Transfer)) and CP-DiscoFlux(with transfer), respectively. CP-DiscoFlux (dashed and dotted curves) exhibits more hardening behavior than the CP-Local model, because of the back stress associated with the pileup of GNDs at the GB. This hardening is slightly reduced for the case where there is finite transmission of dislocation density across the GB (dotted curve) in comparison to the case with zero dislocation transmission (dashed curve). It can be seen that dislocation transport not only gives rise to additional material hardening in comparison to the CP-Local in both cases of CP-DiscoFlux, but there is also additional hardening in comparison to the CP-DiscoFlux results shown for the previous single crystal simulations (Figure 4(b)). This extra hardening can be attributed to the presence of the GB. The GB prevents the free glide of dislocations resulting in the accumulation or depletion of dislocation density at the GB. It can also be seen there is less hardening when dislocation transfer across the GB is considered compared to when it is not. This is due to the fact that as dislocations get transferred across the GB to the appropriate slip system, those dislocations continue to glide and thus, continue to contribute to the plastic dissipation of the energy based on the local stress state of the material. This in turn correlates to less hardening when compared to the case where the GB is impenetrable.

Figure 11 shows the spatial distribution of the negative edge dislocation density in the specimen for the 1st slip system (ρ_{\perp}^{01}) at the macroscopic strain of $\epsilon_{yy} = 0.01$. The comparison is shown between when dislocation transfer across the GB is not considered, Figure 11(a), versus when it is considered, Figure 11(b). The asymmetric distribution of dislocation of opposite polarity gives rise to the development of net polarity of dislocation near the GB. The accumulation/depleting of dislocation density near the

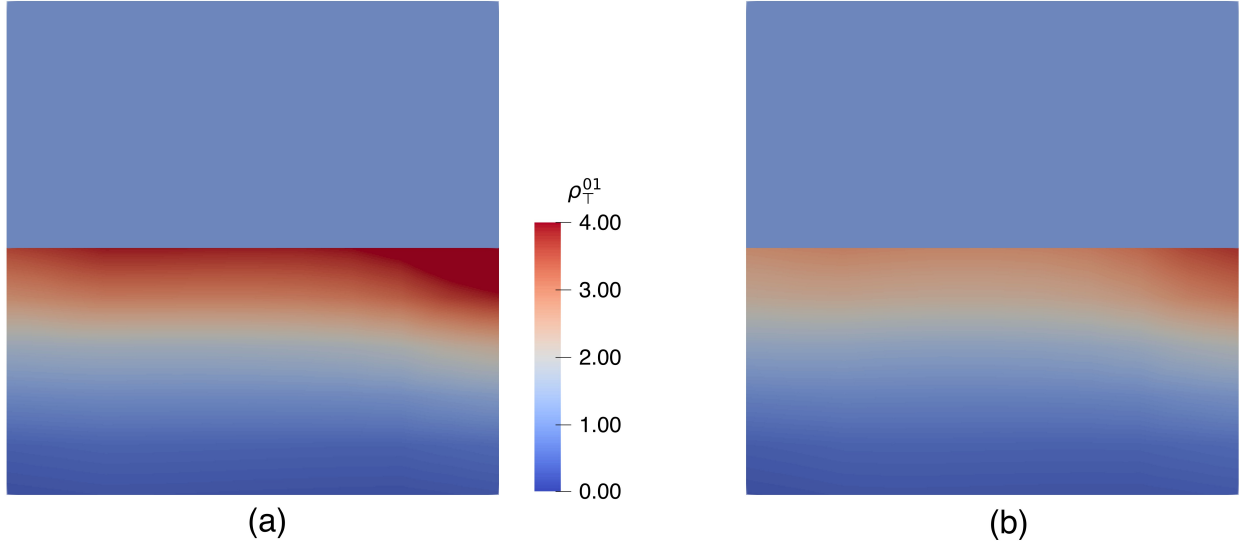


Figure 11: Spatial distribution of the negative edge dislocation density (a) without and (b) with dislocation transfer across the GB on the 1st slip system under compressive loading in a bi-crystal using DiscoFlux at the macroscopic strain of $\epsilon_{yy} = 0.01$. The magnitude of the dislocation density is normalized by the initial dislocation density, $\rho_0 = 1.0 \times 10^6 \text{ mm}^{-2}$

GB is more prominent when dislocation transfer across the GB is not considered. When dislocation transfer across the GB is considered, there is significant reduction in the piling up of dislocation density at the GB, as shown in Figure 11. As dislocations get transferred across the GB to an appropriate slip system, those dislocation further contributes in the plastic deformation of the material. This enhanced plastic slip from the transferred dislocations contributes to the softening of the material as have seen in the volume averaged stress-strain response in Figure 10(b). The top grain in Figure 11 does not show any segregation of dislocation density on 1st slip system because this slip system is not active in Grain B.

To understand the effect of the dislocation transfer across the GB, Figure 12 shows the spatial distribution of GND density, κ_e^{01} when dislocation transfer across the GB is not considered versus when it is considered. It can be seen from Figure 12(a) and Figure 12(b) that due to the incorporation of the dislocation transfer across GB in the second case, the GND accumulation at the GB is significantly lower.

Due to the accumulation of GNDs at the GB, there is significant difference in the development of the back stress. Figure 13 shows the spatial distribution of back stress on the 1st slip system, τ_b^{01} . It can be seen that the development of back stress near the bottom of the sample is very similar when dislocation transfer across GB is considered versus when it is not. However, there is a significant difference at the GB. In fact, when dislocation transfer across the GB is not considered, the GB acts as completely impenetrable to dislocation density transfer and the magnitude of back stress increases to ~ 80 MPa. On the other hand, when dislocation density transfer across the GB is accounted for, the back stress drops to ~ 20 MPa near the GB.

The field distribution of GND density and back stress shown in Figures 12 and

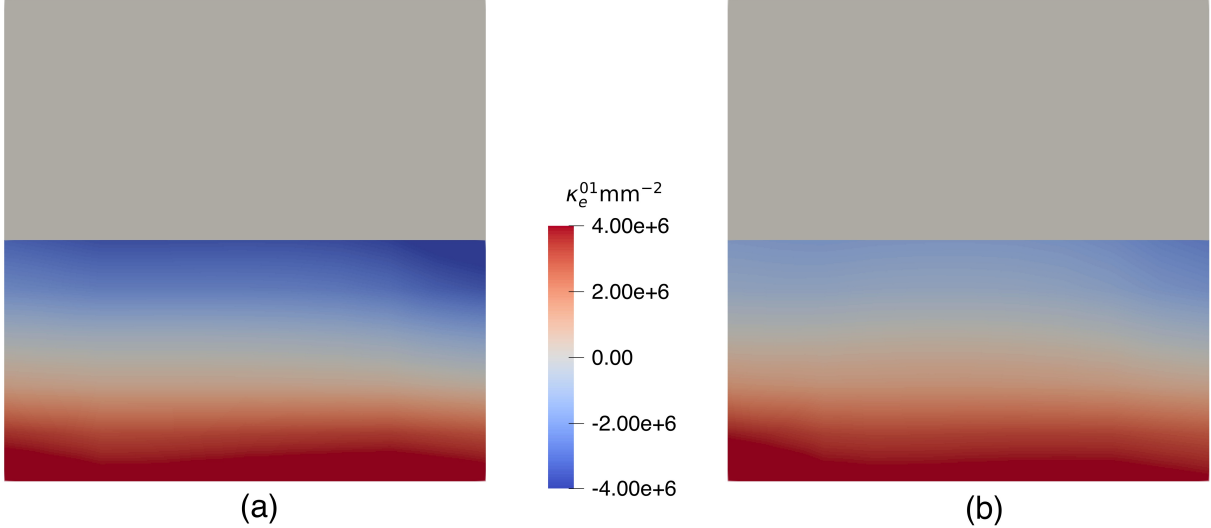


Figure 12: Spatial distribution of the GND density, κ_e^{01} (a) without and (b) with dislocation transfer across the GB on the 1st slip system under compressive loading in a bi-crystal using DiscoFlux at a macroscopic strain of $\epsilon_{yy} = 0.01$.

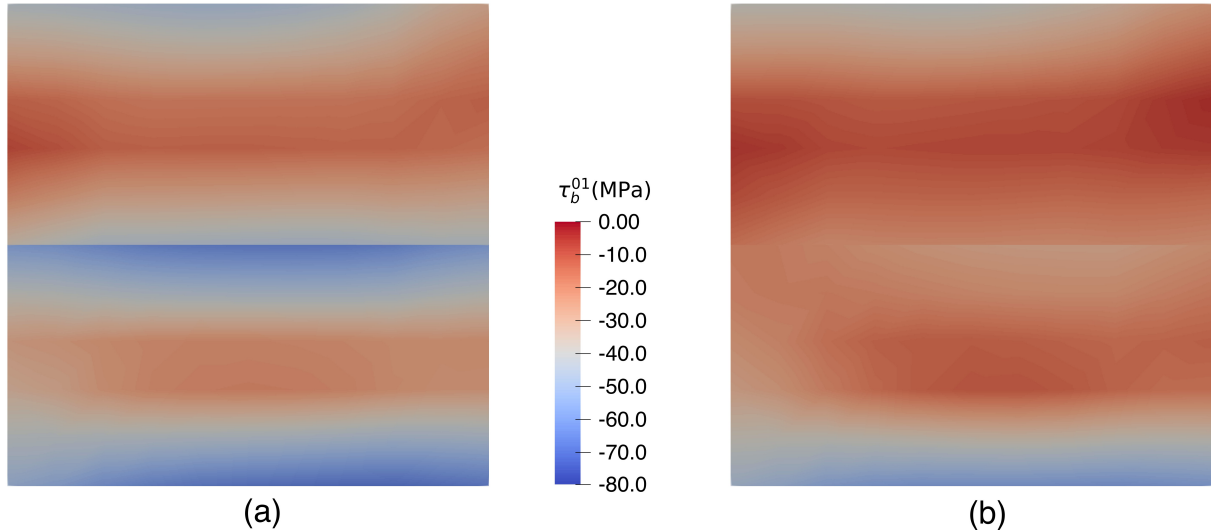


Figure 13: Spatial distribution of the back stress, τ_b^{01} (a) without and (b) with dislocation transfer across the GB on 1st slip system under compressive loading in a bi-crystal using DiscoFlux at a macroscopic strain of $\epsilon_{yy} = 0.01$.

13, respectively, are for edge dislocation density on the 1st slip system. A similar distribution also emerges on other active slip systems. As we can see in Figure 12, in the top grain the GND density is zero. The reason for this is that the 1st slip system is not active in the top grain. Despite zero GND density, there is non-zero back stress on the 1st slip system of the top grain due to the coupling between other slip systems according to equation 26.

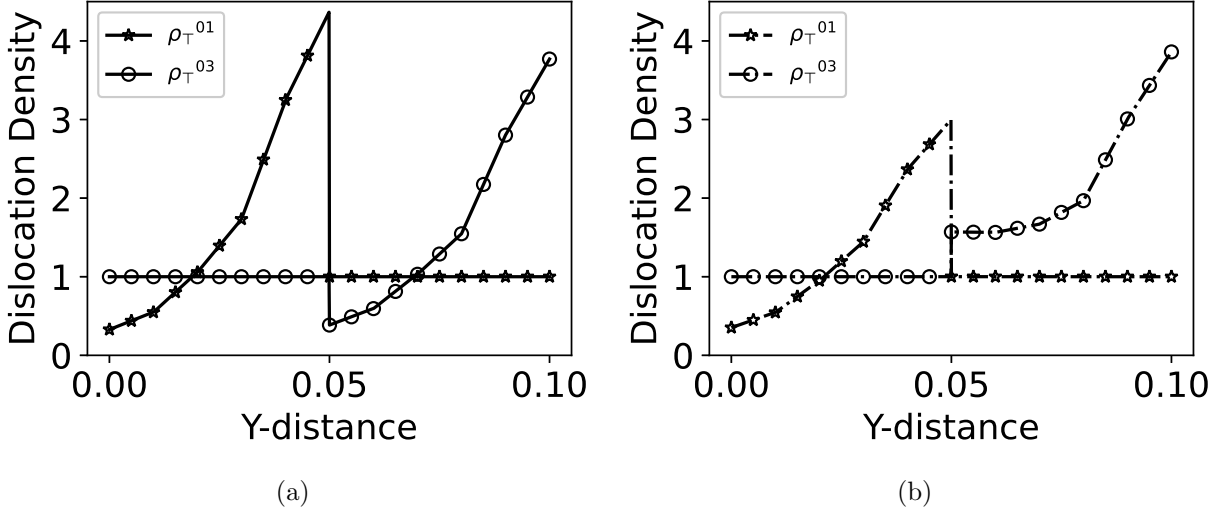


Figure 14: Distribution of negative edge dislocation density on the 1st (ρ_T^{01}) and 3rd (ρ_T^{03}) slip systems along the vertical line through the middle of the sample. DiscoFlux (a) without and (b) with dislocation transfer across the GB at a macroscopic strain of $\epsilon_{yy} = 0.01$. Magnitude of the dislocation density is normalized by the initial dislocation density $\rho_0 = 1.0 \times 10^6 \text{ mm}^{-2}$.

To understand the dislocation activity at the GB, it is worth investigating the dislocation density transfer between different slip systems. For this purpose we use the interaction matrix provided in Figure 2(c) to determine the direction of dislocation flow at the GB. From that interaction matrix, it can be seen that if there is accumulation of dislocation density on slip system 1 at the GB in Grain A, those dislocations are most likely to transfer onto slip system 3 of Grain B. Figure 14 shows the spatial distribution of positive edge dislocation density along a vertical line through the middle of the specimen for slip systems 1 and 3. It can be seen from Figure 14(a and b) that there is a significant difference in the distribution of dislocation density on the 1st and 3rd slip systems due to whether or not dislocation density transfer across the GB is considered. In fact, it can be seen from Figure 14(b) that when dislocation transfer across the GB is considered, the maximum dislocation density accumulation due to dislocation pile-up is $\sim 3 \times 10^6 \text{ mm}^{-2}$. This is not the situation when dislocation transfer across the GB is not considered. Rather in this case, dislocations at the GB keep accumulating without any bound. This difference is because some of the dislocations on 1st slip system in Grain A are transferred to the 3rd slip system of Grain B when transfer is allowed.

It can also be seen from Figure 14(a) that when dislocation transfer across the GB is not considered, the negative edge dislocation density on the 3rd slip system in Grain B gets depleted due to the transportation of dislocation away from the GB. Hence, the negative edge dislocation density of slip system 3 near the GB in Grain B is reduced below the initial dislocation density. When transfer across the GB is activated, the dislocation density on slip system 3 is replenished via transfer from slip system 1 and remains above the initial dislocation density. The relative difference between the dislocation density of the incoming and outgoing slip system at the GB depends on the relative magnitude of dislocation velocity on those slip systems projected perpendicular

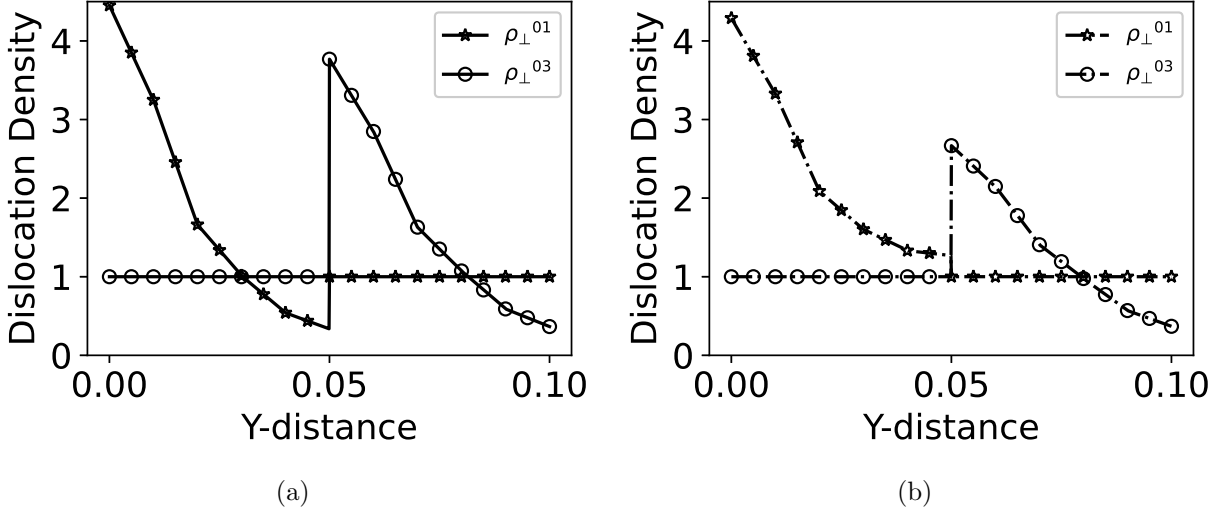


Figure 15: Distribution of positive edge dislocation density on 1st (ρ_{\perp}^{01}) and 3rd (ρ_{\perp}^{03}) slip systems along a vertical line through the middle of the sample using DiscoFlux (a) without and (b) with dislocation transfer across the GB at a macroscopic strain of $\epsilon_{yy} = 0.01$. Magnitude of the dislocation density is normalized to initial dislocation density, $\rho_0 = 1.0 \times 10^6 \text{ mm}^{-2}$.

to the GB plane.

Since positive and negative dislocation densities on a slip system get transported in the opposite directions, a similar but opposite situation arises for positive edge dislocations as shown in Figure 15. It can be seen from Figure 15(a) that a depletion of positive edge dislocation density on the 1st slip system is observed in Grain A when dislocation transfer across the GB is not considered. Similarly, an accumulation of negative edge dislocation on the 3rd slip system in Grain B is observed. When dislocation transfer across the GB is considered, Figure 15(b), there is a significant reduction in the intensity of both the accumulation and depletion near the GB.

The effect of dislocation transfer across the GB can also be realized by inspecting the GND density and back stress in the vicinity of the GB as shown in Figure 16 at a macroscopic strain of $\epsilon_{yy} = 0.01$. Figure 16(a) shows that the magnitude of the GND density near the GB is reduced from $\sim 4 \times 10^6 \text{ mm}^{-2}$ when dislocation transfer is not considered to $\sim 1 \times 10^6 \text{ mm}^{-2}$ when transfer is considered. A similar trend is observed for the back stress in Figure 16(b). The magnitude of the back stress near the GB is reduced from $\sim 80 \text{ MPa}$ when dislocation transfer is not considered to $\sim 30 \text{ MPa}$ when transfer is considered.

3.3 A polycrystal sample under compressive loading

In the bi-crystal example problem discussed above, we have seen the effect of the presence of an interface in the form of a GB that hinders the free movement of dislocations within the sample. In this section, we report on results for a polycrystalline sample test problem that contains several grains with grain size of $100\mu\text{m}$ to $200\mu\text{m}$, which is more representative of experimental samples.

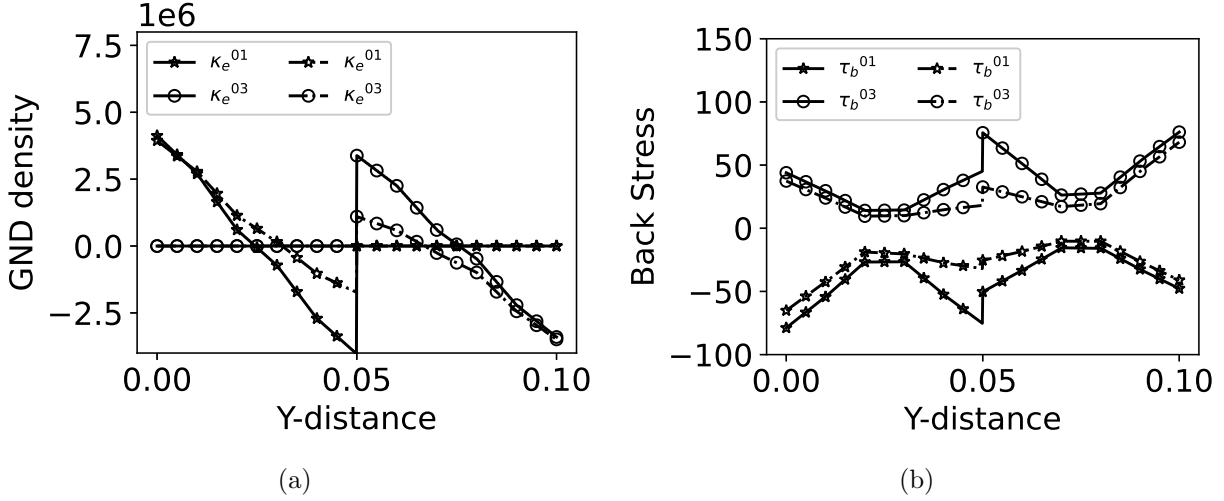


Figure 16: Comparison of the distribution of (a) GND density and (b) back stress of slip system 1 and 3 along a vertical line through the middle of the sample at a macroscopic strain of $\epsilon_{yy} = 0.01$. Dashed lines represent when dislocation transfer across the GB is not considered and dotted lines indicates cases in which it is considered.

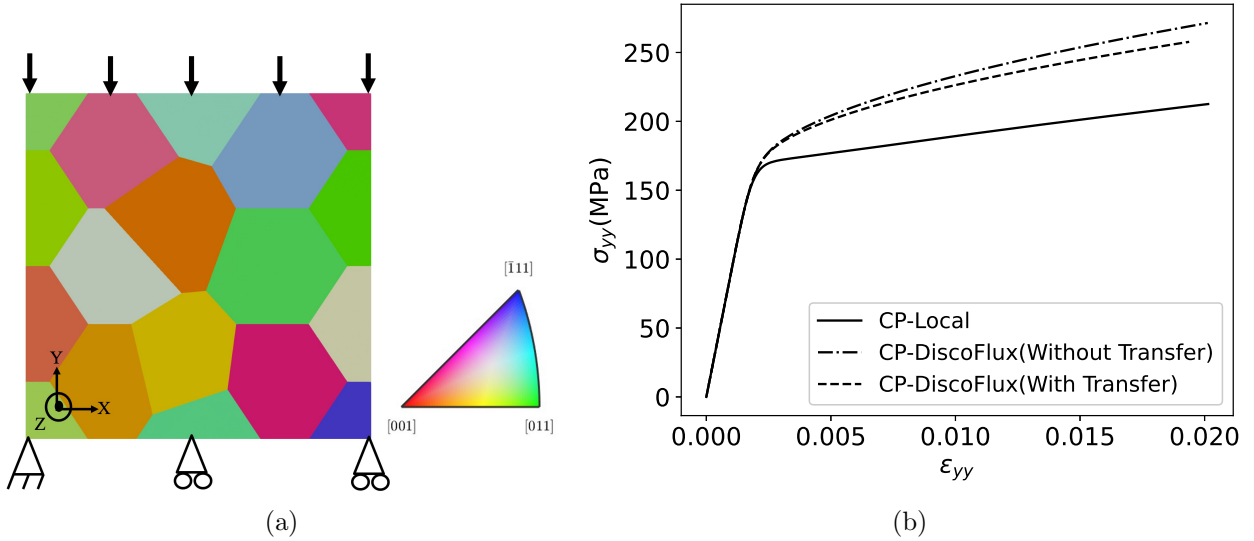


Figure 17: (a) The problem set-up for polycrystalline sample. Grains are colored based on the Inverse Pole Figure. (b) Evolution of the volume averaged stress (σ_{yy}) with respect to the strain (ϵ_{yy}).

Figure 17(a) shows the problem setup for a polycrystalline sample. The polycrystalline sample consists of eighteen grains each with a randomly assigned crystal orientation sampled from $SO(3)$. Again, similar to previous cases, a fixed and roller displacement boundary condition is applied at the bottom surface, and the top surface is compressed at constant rate of $\dot{\epsilon} = 0.1 s^{-1}$ as shown in figure 17(a). A free-flow

boundary condition is applied to all the external surfaces, which implies an assumption that the external surface of the specimen is in essence not a GB rather continuation of the grain. Figure 17(b) shows the volume averaged stress versus strain curve. To understand the effect of dislocation transfer within the grain and across the GB, we compare the response of CP-Local and CP-DiscoFlux. Within CP-DiscoFlux, we also compare the results without transfer and with transfer of dislocation across the GB. Both the CP-Local and CP-DiscoFlux models show significant hardening due to the presence of multiple interfaces in the form of GBs. The hardening slope of both variants of the CP-DiscoFlux model is higher in comparison to the CP-Local, as expected, due to the development of GND density near the grain boundaries and hence the back stress. On the other hand, when dislocation transfer across the GB is considered there is slight softening in comparison to when dislocation transfer across the GB is not considered. This softening can be attributed to the mechanism of dislocation transfer across the GB. Due to the consideration of dislocation transfer across the GB, the GB becomes semi-permeable to the dislocation and the amount of dislocation flux that gets transferred across the GB depends on the accumulation intensity of dislocations at the GB and the stress state of the material near the GB.

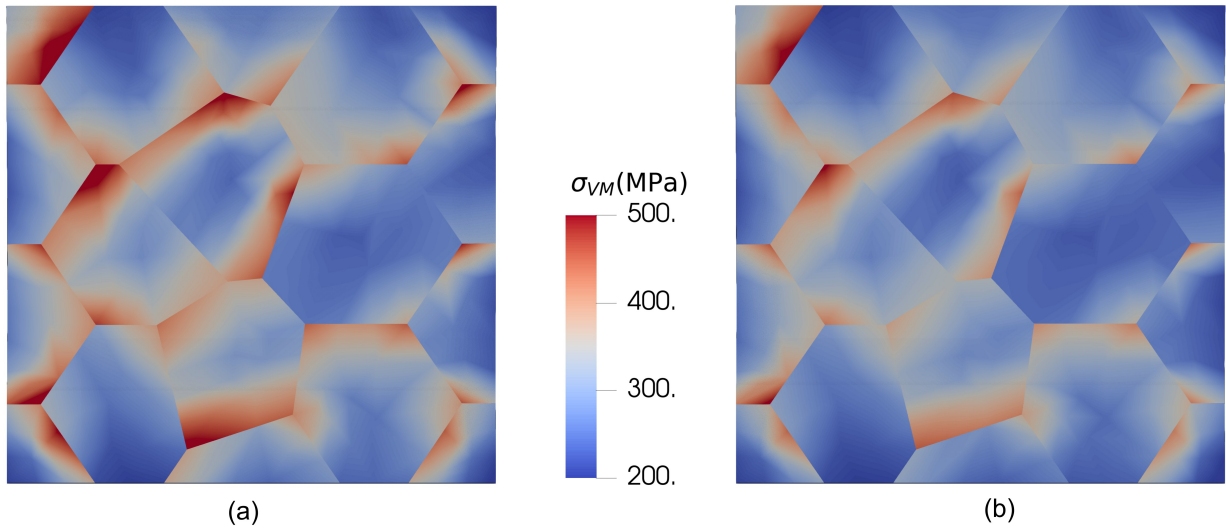


Figure 18: Spatial distribution of the Von-Mises stress under compressive loading in a polycrystal using ‘CP-DiscoFlux’ model with dislocation transfer across the GB is (a) not considered versus when (b) considered. Data is at volume averaged macroscopic strain $\epsilon_{yy} = 0.02$.

The macroscopic softening of the material due to the dislocation transfer across the GB can be better understood by inspecting the field distribution of the von-Mises stress in the polycrystal sample. Figure 18 shows the spatial distribution of the von-Mises stress in the polycrystal sample for ‘CP-DiscoFlux’ models. Owing to the grain misorientation the polycrystal sample inherently develops a heterogeneous distribution of stress. This heterogeneity is further amplified due to the physical transport of dislocations within the grain and the subsequent development of the back stress as shown in Figure 18(a). There is significant stress concentration near the GBs and even more near the triple junctions. But when dislocation transfer across the GB

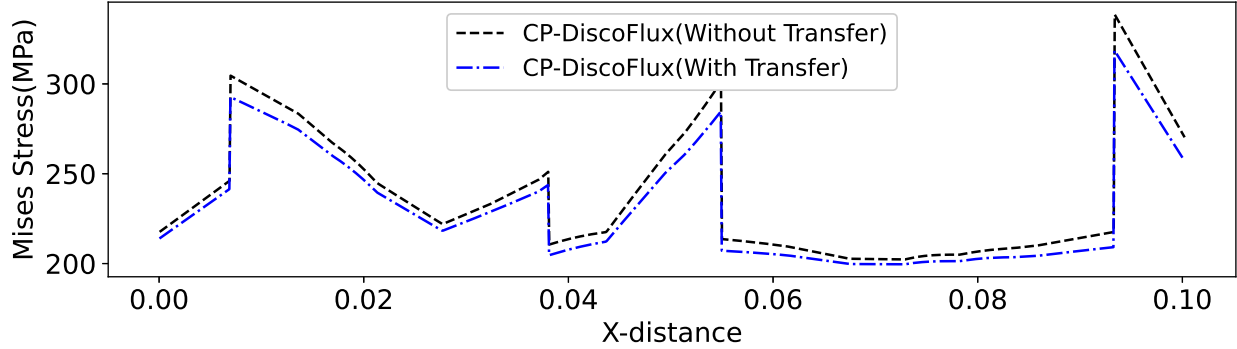


Figure 19: Distribution of von-Mises stress along the horizontal line through the middle of the polycrystal sample using ‘CP-DiscoFlux’ model at volume averaged macroscopic strain $\epsilon_{yy} = 0.02$.

is considered, the stress concentration is less as can be seen in 18(b). It is more evident when the von-Mises stress is inspected along the horizontal line through the middle of the specimen as shown in Figure 19. The von-Mises stress is always less when dislocation transferred across the GB is allowed vs when it is not. The relative difference in magnitude of von-Mises stress is more prominent near the GBs.

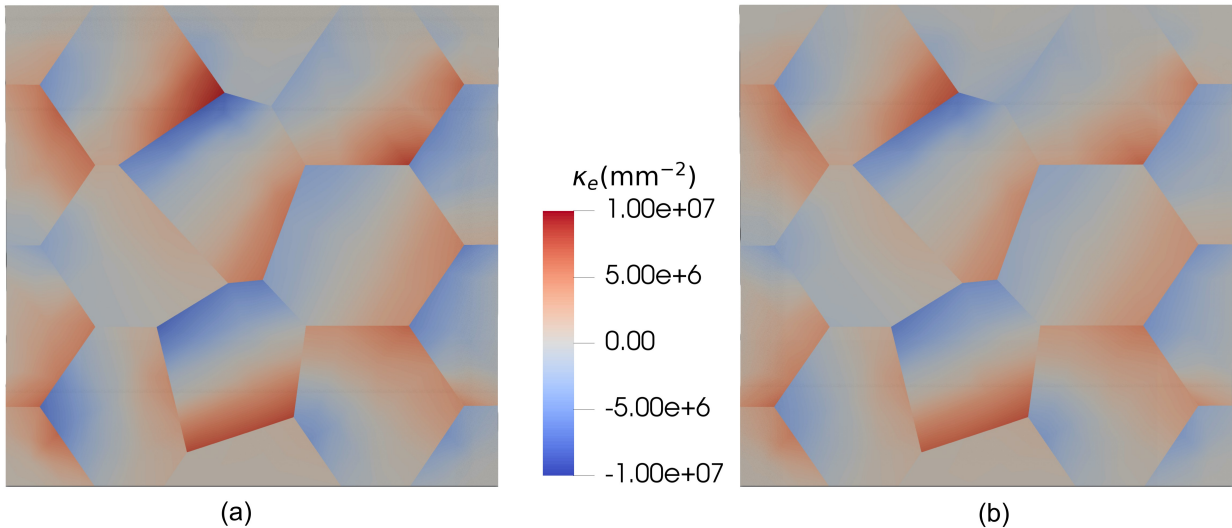


Figure 20: Spatial distribution of the total GND under compressive loading in a polycrystal using ‘CP-DiscoFlux’ model with dislocation transfer across the GB is (a) not considered and (b) considered. Data is at volume averaged macroscopic strain $\epsilon_{yy} = 0.02$.

This reduction in stress concentration can be understood by inspecting the field distribution of GND density in the polycrystal sample mainly near the GBs as shown in Figure 20. It can be seen from 20 (a) and (b) that though the pattern of the development of GND density within the sample remain same but there is difference in the magnitude of GND density. The difference in magnitude is more prominent

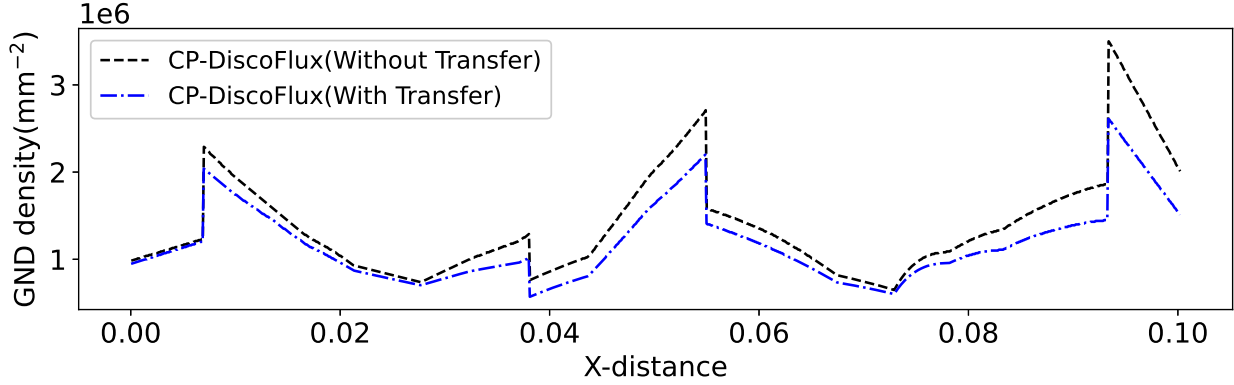


Figure 21: Distribution of total GND density along the horizontal line through the middle of the polycrystal sample using ‘CP-DiscoFlux’ model at volume averaged macroscopic strain $\epsilon_{yy} = 0.02$.

when the GND density is inspected along the horizontal line through the middle of the sample as shown in Figure 21. Along that line, the maximum GND density reaches to $\approx 3.5e+06 \text{ mm}^{-2}$ when dislocation transfer across the GBs is not considered. But when dislocation transfer across the GBs are considered within the model, the maximum GND density reduces to $\approx 2.4e + 06 \text{ mm}^{-2}$, $\approx 30\%$ reduction in the maximum GND density. The amount of this reduction in GND density is very inhomogeneous across the sample.

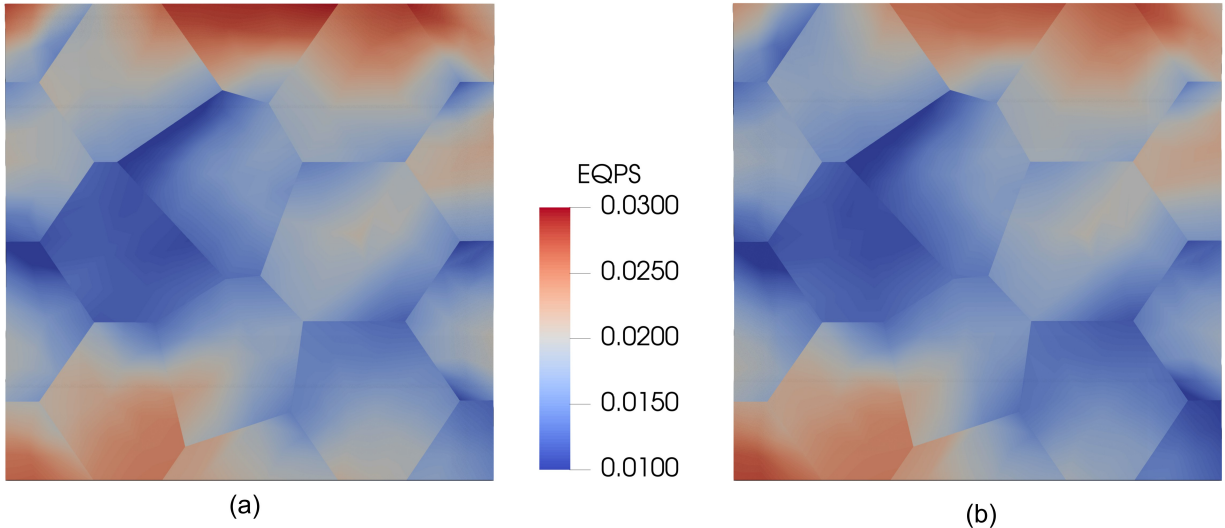


Figure 22: Spatial distribution of the EQPS under compressive loading in a polycrystal using ‘CP-DiscoFlux’ model with dislocation transfer across the GB is (a) not considered and (b) not considered. Data is at volume averaged macroscopic strain $\epsilon_{yy} = 0.02$.

The reduction in GND density has direct consequence in the hardening of the material due to the development of back stress. A large gradient in GND density will

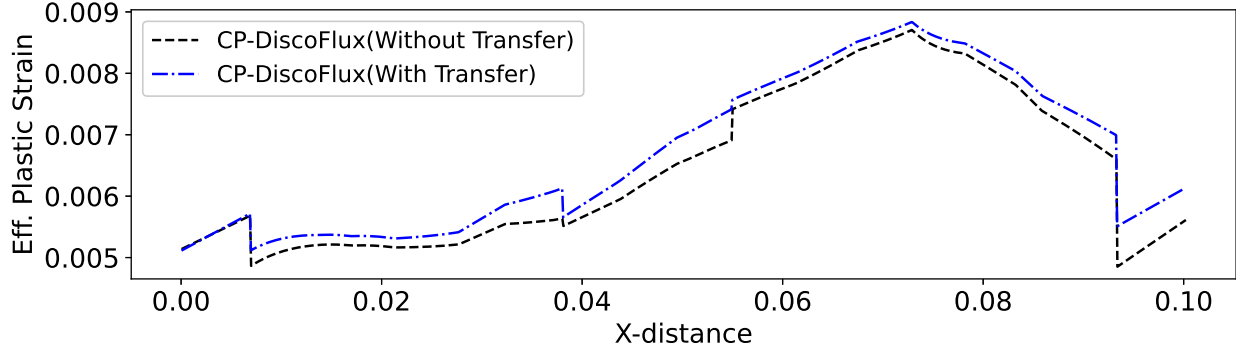


Figure 23: Distribution of equivalent plastic strain along the horizontal line through the middle of the polycrystal sample using ‘CP-DiscoFlux’ model at volume averaged macroscopic strain $\epsilon_{yy} = 0.02$.

give rise to a large back stress. A large back stress will hinder the further polarization of dislocations thus reducing the amount of plastic slip and vice versa. Thus when the GND density reduces due to the dislocation transfer across the GBs, it has direct consequence in the development of plastic strain within the sample. Figure 22 shows the distribution of the equivalent plastic strain(EQPS) within the sample at volume averaged macroscopic strain $\epsilon_{yy} = 0.02$. The effect of dislocation transfer across the GBs on EQPS is more evident when inspected along the horizontal line through the middle of the sample as shown in Figure 23. It can be seen from Figure 21 and Figure 23 that GND density has direct consequence in the development of plastic strain within the material. A high GND density in general leads to the more hardening of the material and thus less plastic strain.

4 Concluding remarks

In the work we have presented a dislocation transport based crystal plasticity model where dislocation transport both within and across grains is directly accounted for. To achieve this, we started with an existing dislocation transport based crystal plasticity model developed in LANL called ‘Discoflux’. In the existing ‘DiscoFlux’ model the grain boundaries are treated either as impermeable to dislocation transfer or completely permeable to dislocation transfer. To develop a proper dislocation transfer criterion across the GB, we explore some of the existing models that are based on geometric features. We have outlined the features and limitations of previous criteria and then developed a new criterion that incorporates all the critical requirements of dislocation transfer across the GB. This new criterion is incorporated within the ‘DiscoFlux’ model.

In the present work the modified ‘DiscoFlux’ model is implemented in the open-source code MOOSE. Implicit time integration scheme is used to integrate the rate equations. The model is in 3D to capture the interaction between dislocations in all slip systems. We have used this implementation to study some of the benchmark problems of single crystal and bi-crystal to verify the implementation. The comparison is made with local crystal plasticity material model i.e., when dislocation transport within and across the GB is not considered. As a verification of the implementation

the local crystal plasticity model was able to capture the uniform stress field in a single crystal under pure shear loading. Next, the material response of single crystal is studied using the newly developed model. The model was able to capture the development of GND density at the impermeable outer boundaries. Subsequent development of back stress and evolution of dislocation density in the most active slip system is analyzed.

Next, to study the effect of GB, we developed a bi-crystal computational domain. Material response of the bi-crystal under compressive loading is studied. Comparison is made in the material response using three material models, (a)local crystal plasticity, (b) 'DiscoFlux' model with only dislocation transport within the grain and (c) 'DiscoFlux' model with dislocation transfer within the grain as well as across the GB. Extra material hardening due to the development of back stress was captured by both the 'DiscoFlux' models. Model was also able to capture slight softening in the material response due to the transfer of dislocation across the GB. For detail understanding of the dislocation flow at the GB, the evolution of dislocation density in the most active slip-system in both the grains are analysed. A significant reduction in dislocation pile-up as well as GND density and back stress is observed at the GB.

Next, material response of a polycrystalline domain under compressive loading is studied. The polycrystalline domain contains many grain boundaries, which are potential source as barrier for free movement of dislocation and hence location for dislocation pile-up and stress concentration. The 'DiscoFlux' model was able to capture the development of GND density near the grain boundaries and triple junctions. Subsequent local hardening of the material due to the transport of dislocation within the grain and slight softening due to dislocation transfer across the GB is also captured. Spatial evolution of some of the important state variables e.g., von-Mises stress, GND density and Equivalent Plastic Strain(EQPS) are analyzed.

We have demonstrated the effect of physical transport of dislocations within the grain and across the GB in crystal plasticity model. The framework to transfer dislocation across the GB is general enough to tune it for other materials with different crystal structures. The next extension of the model includes a detail experimental calibration and validation for a particular material. The knowledge from this validation effort will provide crucial information regarding the required modification that might be needed to tune the model for more complex material e.g., multi-component alloys.

Acknowledgement

The computation resources and support provided by the High Performance Computing (HPC) division at Los Alamos National Laboratory is greatly acknowledged.

Authors wants to thank the funding from LDRD-DR "Investigating How Material's Interfaces and Dislocations Affect Strength" (iMIDAS) under grant no. 20210036DR. The Los Alamos National Laboratory is operated by the Triad National Security,LLC, for the National Nuclear Security Administration of U.S. Department of Energy (Contract No. 89233218CNA000001).

A Slip System Convention

In the present work, fcc copper has been used as the representative material. The slip system information for an fcc material and the index used in the present work is provided in Table 3.

Slip System Index	Slip Plane Normal	Slip Direction
1	[1,1,̄1]	[0,1,1]
2	[1,1,̄1]	[1,0,1]
3	[1,1,̄1]	[1,̄1,0]
4	[1,̄1,̄1]	[0,1,̄1]
5	[1,̄1,̄1]	[1,0,1]
6	[1,̄1,̄1]	[1,1,0]
7	[1,̄1,1]	[0,1,1]
8	[1,̄1,1]	[1,0,̄1]
9	[1,̄1,1]	[1,1,0]
10	[1,1,1]	[0,1,̄1]
11	[1,1,1]	[1,0,̄1]
12	[1,1,1]	[1,̄1,0]

Table 3: Slip system index along with slip plane normal and slip direction used in the present work.

References

- [1] T.R. Bieler, R. Alizadeh, M. Peña-Ortega, and J. Llorca. An analysis of (the lack of) slip transfer between near-cube oriented grains in pure Al. *International Journal of Plasticity*, 118:269–290, July 2019.
- [2] T.R. Bieler, P. Eisenlohr, C. Zhang, H.J. Phukan, and M.A. Crimp. Grain boundaries and interfaces in slip transfer. *Current Opinion in Solid State and Materials Science*, 18(4):212–226, August 2014.
- [3] Josh Kacher, B.P. Eftink, B. Cui, and I.M. Robertson. Dislocation interactions with grain boundaries. *Current Opinion in Solid State and Materials Science*, 18(4):227–243, August 2014.
- [4] Josh Kacher and I.M. Robertson. Quasi-four-dimensional analysis of dislocation interactions with grain boundaries in 304 stainless steel. *Acta Materialia*, 60(19):6657–6672, November 2012.
- [5] F. Roters, P. Eisenlohr, L. Hantcherli, D.D. Tjahjanto, T.R. Bieler, and D. Raabe. Overview of constitutive laws, kinematics, homogenization and multiscale methods in crystal plasticity finite-element modeling: Theory, experiments, applications. *Acta Materialia*, 58(4):1152–1211, February 2010.
- [6] S.R. Kalidindi, C.A. Bronkhorst, and L. Anand. Crystallographic texture evolution in bulk deformation processing of FCC metals. *Journal of the Mechanics and Physics of Solids*, 40(3):537–569, January 1992.
- [7] L. Anand and M. Kothari. A computational procedure for rate-independent crystal plasticity. *Journal of the Mechanics and Physics of Solids*, 44(4):525–558, April 1996.
- [8] Shahriyar Keshavarz, Somnath Ghosh, Andrew C.E. Reid, and Stephen A. Langer. A non-Schmid crystal plasticity finite element approach to multi-scale modeling of nickel-based superalloys. *Acta Materialia*, 114:106–115, August 2016.
- [9] Thao Nguyen, D.J. Luscher, and J.W. Wilkerson. A dislocation-based crystal plasticity framework for dynamic ductile failure of single crystals. *Journal of the Mechanics and Physics of Solids*, 108:1–29, November 2017.
- [10] D.J. Luscher, J.R. Mayeur, H.M. Mourad, A. Hunter, and M.A. Kenamond. Coupling continuum dislocation transport with crystal plasticity for application to shock loading conditions. *International Journal of Plasticity*, 76:111–129, January 2016.
- [11] Jason R Mayeur, Hashem M Mourad, Darby J Luscher, Abigail Hunter, and Mark A Kenamond. Numerical implementation of a crystal plasticity model with dislocation transport for high strain rate applications. *Modelling and Simulation in Materials Science and Engineering*, 24(4):045013, May 2016.
- [12] Sarra Haouala, Javier Segurado, and Javier LLorca. An analysis of the influence of grain size on the strength of FCC polycrystals by means of computational homogenization. *Acta Materialia*, 148:72–85, April 2018.
- [13] S. Haouala, R. Alizadeh, T.R. Bieler, J. Segurado, and J. LLorca. Effect of slip transmission at grain boundaries in Al bicrystals. *International Journal of Plasticity*, 126:102600, March 2020.

- [14] Doris Kuhlmann-Wilsdorf. Dislocation cells, redundant dislocations and the leds hypothesis. *Scripta Materialia*, 34(4):641–650, February 1996.
- [15] J. A. Hurtado and J. Weertman. Non-redundant dislocation density field of a circular bar deformed in torsion and the stress gradient hardening effect. *physica status solidi (a)*, 149(1):173–186, 1995.
- [16] Yinguang Piao and Khanh Chau Le. Thermodynamic theory of dislocation/grain boundary interaction. *Continuum Mechanics and Thermodynamics*, 34(3):763–780, May 2022.
- [17] Derek Gaston, Chris Newman, Glen Hansen, and Damien Lebrun-Grandié. MOOSE: A parallel computational framework for coupled systems of nonlinear equations. *Nuclear Engineering and Design*, 239(10):1768–1778, October 2009.
- [18] PETSc web page. <https://petsc.org/>, 2023.
- [19] Satish Balay, William D. Gropp, Lois Curfman McInnes, and Barry F. Smith. Efficient Management of Parallelism in Object-Oriented Numerical Software Libraries. In Erlend Arge, Are Magnus Bruaset, and Hans Petter Langtangen, editors, *Modern Software Tools for Scientific Computing*, pages 163–202. Birkhäuser Boston, Boston, MA, 1997.
- [20] U. F. Kocks, Ali S. Argon, and M. F. Ashby. *Thermodynamics and Kinetics of Slip*. Number v. 19 in Progress in Materials Science. Pergamon Press, Oxford ; New York, 1st ed edition, 1975.
- [21] Athanasios Arsenlis and David M. Parks. Modeling the evolution of crystallographic dislocation density in crystal plasticity. *Journal of the Mechanics and Physics of Solids*, 50(9):1979–2009, September 2002.
- [22] A.H. Cottrell. The formation of immobile dislocations during slip. *The London, Edinburgh, and Dublin Philosophical Magazine and Journal of Science*, 43(341):645–647, June 1952.
- [23] N.A Fleck, M.F Ashby, and J.W Hutchinson. The role of geometrically necessary dislocations in giving material strengthening. *Scripta Materialia*, 48(2):179–183, January 2003.
- [24] M. F. Ashby. The deformation of plastically non-homogeneous materials. *The Philosophical Magazine: A Journal of Theoretical Experimental and Applied Physics*, 21(170):399–424, February 1970.
- [25] Ryan A. Austin and David L. McDowell. A dislocation-based constitutive model for viscoplastic deformation of fcc metals at very high strain rates. *International Journal of Plasticity*, 27(1):1–24, January 2011.
- [26] U.F. Kocks and H. Mecking. Physics and phenomenology of strain hardening: The FCC case. *Progress in Materials Science*, 48(3):171–273, January 2003.
- [27] B. Devincre, T. Hoc, and L. Kubin. Dislocation Mean Free Paths and Strain Hardening of Crystals. *Science*, 320(5884):1745–1748, June 2008.
- [28] C.J. Bayley, W.A.M. Brekelmans, and M.G.D. Geers. A comparison of dislocation induced back stress formulations in strain gradient crystal plasticity. *International Journal of Solids and Structures*, 43(24):7268–7286, November 2006.

- [29] L Evers. Non-local crystal plasticity model with intrinsic SSD and GND effects. *Journal of the Mechanics and Physics of Solids*, 52(10):2379–2401, October 2004.
- [30] J.D Livingston and B Chalmers. Multiple slip in bicrystal deformation. *Acta Metallurgica*, 5(6):322–327, June 1957.
- [31] Michael D. Sangid, Tawhid Ezaz, Huseyin Sehitoglu, and Ian M. Robertson. Energy of slip transmission and nucleation at grain boundaries. *Acta Materialia*, 59(1):283–296, January 2011.
- [32] E. Bayerschen, A. T. McBride, B. D. Reddy, and T. Böhlke. Review on slip transmission criteria in experiments and crystal plasticity models. *Journal of Materials Science*, 51(5):2243–2258, March 2016.
- [33] Y. Guo, T.B. Britton, and A.J. Wilkinson. Slip band–grain boundary interactions in commercial-purity titanium. *Acta Materialia*, 76:1–12, September 2014.
- [34] J. Luster and M. A. Morris. Compatibility of deformation in two-phase Ti-Al alloys: Dependence on microstructure and orientation relationships. *Metallurgical and Materials Transactions A*, 26(7):1745–1756, July 1995.
- [35] Z. Shen, R.H. Wagoner, and W.A.T. Clark. Dislocation pile-up and grain boundary interactions in 304 stainless steel. *Scripta Metallurgica*, 20(6):921–926, June 1986.
- [36] Z. Shen, R.H. Wagoner, and W.A.T. Clark. Dislocation and grain boundary interactions in metals. *Acta Metallurgica*, 36(12):3231–3242, December 1988.
- [37] M De Koning, R.J Kurtz, V.V Bulatov, C.H Henager, R.G Hoagland, W Cai, and M Nomura. Modeling of dislocation–grain boundary interactions in FCC metals. *Journal of Nuclear Materials*, 323(2-3):281–289, December 2003.
- [38] Maurice De Koning, R. Miller, V. V. Bulatov, and Farid F. Abraham. Modelling grain-boundary resistance in intergranular dislocation slip transmission. *Philosophical Magazine A*, 82(13):2511–2527, September 2002.
- [39] Michael Waskom. Seaborn: Statistical data visualization. *Journal of Open Source Software*, 6(60):3021, April 2021.
- [40] H.-J. Bunge. *Texture Analysis in Materials Science: Mathematical Methods*. Elsevier Science, Cambridge, 2014.
- [41] Sicong He, Emily H. Mang, Asher C. Leff, Xinran Zhou, Mitra L. Taheri, and Jaime Marian. Complex dislocation loop networks as natural extensions of the sink efficiency of saturated grain boundaries in irradiated metals. *Science Advances*, 10(18):eadj8395, May 2024.
- [42] Farhan Javaid, Habib Pouriayevali, and Karsten Durst. Dislocation–grain boundary interactions: Recent advances on the underlying mechanisms studied via nanoindentation testing. *Journal of Materials Research*, 36(12):2545–2557, June 2021.
- [43] Vilgeir Dalen. Simplified Finite-Element Models for Reservoir Flow Problems. *Society of Petroleum Engineers Journal*, 19(05):333–343, October 1979.
- [44] K. M. Jassby and T. Vreeland. Dislocation Mobility in Pure Copper at 4.2 °K. *Physical Review B*, 8(8):3537–3541, October 1973.

- [45] James Ahrens, Berk Geveci, and Charles Law. ParaView: An End-User Tool for Large-Data Visualization. In *Visualization Handbook*, pages 717–731. Elsevier, 2005.
- [46] S. Yefimov and E. Van Der Giessen. Multiple slip in a strain-gradient plasticity model motivated by a statistical-mechanics description of dislocations. *International Journal of Solids and Structures*, 42(11-12):3375–3394, June 2005.